192 (2024) 206935

Contents lists available at ScienceDirect

Applied Catalysis O: Open

journal homepage: www.elsevier.com/locate/apcato

# The catalytic activity of bimetallic FeCoBEA zeolite catalysts in Fischer-Tropsch synthesis – The role of cobalt in framework position of dealuminated SiBEA zeolite

Karolina A. Chałupka-Śpiewak [a,*], Jacek Gurgul [b], Jacek Grams [a], Paweł Mierczyński [a], Waldemar Maniukiewicz [a], Małgorzata I. Szynkowska-Jóźwik [a], Kazimierz Łątka [c], Jacek Rynkowski [a], Stanisław Dźwigaj [d,*]

[a] Lodz University of Technology, Faculty of Chemistry, Institute of General and Ecological Chemistry, Zeromskiego 116, 90-924 Lodz, Poland
[b] Jerzy Haber Institute of Catalysis and Surface Chemistry, Polish Academy of Sciences, Niezapominajek 8, 30-239 Krakow, Poland
[c] M. Smoluchowski Institute of Physics, Jagiellonian University, Łojasiewicza 11, 30-348 Krakow, Poland
[d] Laboratoire de Reactvite de Surface, Sorbonne-Universite, CNRS, UMR 7197, 4 Place Jussieu, Tour 43-53, 75005 Paris, France

ARTICLE INFO

*Keywords:*
BEA zeolite
Fischer-Tropsch synthesis
Cobalt catalysts
iron catalysts
Bimetallic iron-cobalt catalysts

ABSTRACT

Two series of BEA zeolite modified with transition metals (Co and Fe) with different metals loadings were obtained: the first one was prepared by classical sequential wet impregnation to obtain C-$Fe_xCo_y$AlBEA catalysts; the second one was obtained by a two-step postsynthesis method to design C-$Fe_xCo_y$SiBEA catalysts. The catalytic activity of both series of FeCoBEA zeolite catalysts was determined by the FTS process. These bimetallic catalysts appear to combine the advantages of monometallic cobalt catalysts (lower selectivity towards $CO_2$ than for monometallic iron catalysts) and iron catalysts (lower selectivity towards $CH_4$ than for monometallic cobalt catalysts), while minimizing their disadvantages, such as the large amount of carbon deposition.

## 1. Introduction

The Fischer-Tropsch synthesis is known since 1920 when these two German scientists discovered and optimized the possibility of obtaining fuel from synthesis gas [1]. During this synthesis the ultra-clean, sulfur and nitrogen-free chemicals and fuels can be produced. The source of synthesis gas can be gasification of natural gas, coal or biomass. Depending on the source of syngas, three technologies can be distinguished: CTL – coal to liquid, GTL – gas to liquid, BTL – biomass to liquid [2 – 5]. For many years, the synthesis pioneered by Franz Fischer and Hans Tropsch has been developed by scientists around the world, as evidenced by numerous publications on FTS. There has been a particular increase in interest in this topic since 2004, since when the number of publications has steadily increased. Such a rapid growth in interest in FTS is a consequence of the depletion of oil resources and the protection of the environment, which is constantly being destroyed, but also the global demand for fuels and global transportation and environmental policies regarding air quality and vehicle exhaust fumes emitted into the atmosphere [6]. FTS seems to be a good solution to these requirements. However, this synthesis also comes with a number of challenges that need to be solved for better industrial application.

The Fischer-Tropsch process is carried out using catalysts. Typically, cobalt or iron is used as the active phase and is supported by various carriers such as silica or alumina, zeolites, mesoporous materials and molecular sieves, titanium oxides, activated carbon, *etc.* It has been reported that the type of products in the FTS process depends on the active component of the catalysts, as well as the reaction conditions used. The catalytic properties may depend on the size of the active particles in the catalytic systems, so designing active, selective and stable catalysts for FTS is still a huge challenge for researchers [7]. It is now well known that monometallic cobalt catalysts are highly active and preferred in the gas-to-liquid (GTL) FTS process, since the use of this type of catalyst leads to the formation of mainly linear paraffins. Alumina-based cobalt catalysts are currently used at Qatar Petroleum-Sasol GLT plant [6,8]. Advantages of cobalt include the use of lower reaction temperatures and low activity of these catalysts in the WGS reaction, as well as less methane produced in FTS, which is an undesirable product, allowing the use of syngas with a higher $H_2$/CO ratio. The disadvantages of cobalt

* Corresponding authors.
*E-mail addresses:* karolina.chalupka@p.lodz.pl (K.A. Chałupka-Śpiewak), stanislaw.dzwigaj@sorbonne-universite.fr (S. Dźwigaj).

https://doi.org/10.1016/j.apcato.2024.206935
Received 29 November 2023; Received in revised form 12 April 2024; Accepted 23 May 2024
Available online 29 May 2024

catalysts are the price of the metal and the need to support it on different materials, which can result in the need to control metal-substrate interactions. Strong metal-substrate interactions can lead to low reducibility and thus low activity, and weak interactions (too small) between cobalt and the substrate can lead to agglomeration of cobalt particles and their sintering, which also results in lower CO conversion [6]. Iron catalysts, compared to cobalt catalysts, are cheaper and can operate at higher temperatures and do not require very high quality synthesis gas, which is why they are preferred in coal-to-liquid (CTL) technology [8]. However, the use of iron catalysts for FTS results in the formation of $CH_4$ and greater carbon deposition, and thus faster catalyst deactivation. It is known that the FTS reaction on iron-based catalysts produces olefins and oxidized products [2]. Regardless of the use of active metal in FTS, the sintering of metal particles and enhancement of carbon deposition resistance remains a problem to be solved and a challenge for researchers.

In our earlier works [9 – 11], we reported that the two-step post-synthesis method previously developed by Dzwigaj et al. [12] allows us to obtain highly active monometallic cobalt-iron catalysts for Fischer-Tropsch synthesis, which are resistant to sintering of metal particles and exhibit lower carbon deposition than ordinary carrier catalysts used in FTS. These results encouraged us to study bimetallic catalytic systems and try to combine the advantages of cobalt and iron catalysts while minimizing their disadvantages. In the present work, we present bimetallic iron-cobalt catalysts of BEA zeolites for Fischer-Tropsch synthesis prepared by two different methods: classical wet sequential impregnation and a two-step postsynthesis method which allowed the incorporation of cobalt ions into the framework of BEA zeolite and iron in an extra-framework position. The present work focuses on the differences in the physicochemical properties of two different series of catalysts and the role of cobalt ions located in the framework positions of BEA zeolite and their effect on the activity of bimetallic BEA zeolite catalysts.

## 2. Experimental

### 2.1. Sample preparation

The series of $Fe_xCo_ySiBEA$ and $Fe_xCo_yAlBEA$ (where x = 2.5, 5.0 and 10.0 Fe wt% and y = 2.5, 5.0 and 10.0 Co wt%) zeolites were prepared by, respectively: (i) a two-step postsynthesis procedure and (ii) conventional wet impregnation. Both metals ions in two series of catalysts were impregnated sequentially.

Tetraethylammonium BEA (TEABEA) zeolite supplied by RIPP (China) was divided into two fractions. The first part was calcined (air, 15 h, 550 °C) to obtain organic-free AlBEA zeolite (Si/Al = 12.5). $Fe_xCo_yAlBEA$ zeolites were prepared by sequential wet impregnation of AlBEA. First, an aqueous solution of $Co(NO_3)_2 \cdot 6\ H_2O$ (pH = 2.6; manufacturer by Sigma Aldrich, 99.9% of purity) under aerobic conditions were stirred for 24 h at room temperature, followed by evaporated of water at 80 °C. The dried $Co_yAlBEA$ zeolites samples were then impregnated with an aqueous solution of $Fe(NO_3)_3 \cdot 9H_2O$ (pH = 2.4–2.6; manufacturer by Sigma Aldrich, 99.9% of purity) also under aerobic conditions, the suspensions were stirred for 24 h at room temperature, and then such suspension was dried in an evaporator at 80 °C until the water evaporated. The obtained solids were calcined in air at 500 °C for 3 h and labelled as $C\text{-}Fe_xCo_yAlBEA$.

The second fraction of TEABEA was treated with 13 mol $\cdot L^{-1}$ $HNO_3$ aqueous solution (4 h, 80 °C) to obtain a dealuminated and organic-free SiBEA substrate (Si/Al = 1300) with vacant T-atom sites (where T = Al). SiBEA was then separated by centrifugation, washed with distilled water and dried overnight at 80 °C. To incorporate $Co^{2+}$ ions into vacant T-atom sites, 2 g of SiBEA was stirred under aerobic conditions for 24 h at 25 °C in 200 mL of an aqueous solution of $Co(NO_3)_2{\cdot}6\ H_2O$ (pH = 2.4–2.6) at different concentrations to obtain solids with different Co contents (y = 2.5, 5.0 and 10.0 wt% of Co). The suspensions were then stirred at 80 °C for 2 h until the water evaporated and the resulting solids were air-dried at 80 °C for 24 h and labelled as $Co_ySiBEA$. This was followed by sequential impregnation with an aqueous solution of $Fe(NO_3)_3 \cdot 9H_2O$ (pH = 2.4–2.6) also under aerobic conditions for 24 h at 25 °C in 200 mL of mentioned solution. After mixing the suspensions and evaporating the water at 80 °C, the solids were calcined in air at 500 °C for 3 h and labelled as $C\text{-}Fe_xCo_ySiBEA$.

Prior to FT reaction tests, $C\text{-}Fe_xCo_ySiBEA$ and $C\text{-}Fe_xCo_yAlBEA$ were reduced *in situ* at atmospheric pressure in a flow of 95% $H_2$–5% Ar (Air Liquid, purity 99.999%) stream at 400 °C for 1 h and the catalysts thus obtained were labelled as $Red\text{-}C\text{-}Fe_xCo_ySiBEA$ and $Red\text{-}C\text{-}Fe_xCo_yAlBEA$.

The composition of catalysts was determined by XRF method.

### 2.2. Methods of characterization

#### 2.2.1. XRF

X-Ray Fluorescence Spectroscopy is a non-destructive analytical method and was used to analyze the elemental composition of the samples under study. The analysis of BEA zeolites and samples obtained (as prepared) without high-temperature thermal treatment was carried out using a Spectro Xepos XRF spectrometer (AMETEK Materials Analysis Division). Chemical elements were identified on the basis of their characteristic wavenumber or X-Ray emission energy, the content of a given element was determined by measuring the intensity of its line.

#### 2.2.2. BET

Brunauer-Emmett-Teller method - The specific surface area (SSA) and porosity of the catalysts and their supports were determined using a Micromeritics ASAP 2020 V3.05 G (Surface Area and Porosity Analyzer) automated sorptometer. Samples were prepared at 350 °C during a 4-h evacuation, followed by low temperature nitrogen adsorption-desorption measurements using the BET method (liquid $N_2$). The total surface area was determined by the Brunauer-Emmet-Teller (BET) method. Micropore volumes and micropore area was obtained using t-plot method. To determine adsorption in micropores, the Dubinin-Astakhov method and the Dubinin-Radushkevich model were used to determine the volume of micropores and their adsorption capacity. The Barrett-Joyner-Halenda (BJH) model applied to the adsorption branch of the isotherm was used to obtain size distribution of the mesopores.

#### 2.2.3. XRD

Powder X-ray diffractograms were recorded on a PAN analytical X'Pert Pro MPD instrument using Cu $K_\alpha$ radiation ($\lambda = 154.05$ pm) in the $2\theta$ range from 5 to 90°. Samples after calcination were examined, and their phase composition was determined. Samples after reduction, as well as after FTS reaction, were measured to determine the crystal structure after treatment under severe and hard conditions.

#### 2.2.4. Temperature programmed reduction

TPR-$H_2$ measurements were carried out in an automatic TPR system (AMI-1) in the temperature range of 25–900 °C, using $H_2$ stream (5% $H_2$–95% Ar, manufacturer by Air Liquide, 99.99% of purity, flow rate 40 mL$\cdot$ $min^{-1}$). $H_2$ consumption was monitored using a thermal conductivity detector (TCD). The linear rate of temperature increase was 10 °C$\bullet min^{-1}$.

#### 2.2.5. ToF-SIMS

Time-of-flight secondary ion mass spectrometry (ToF-SIMS) measurements were performed using an ION-TOF GmbH instrument (TOF-SIMS IV) equipped with a 25 kV pulsed $Bi_3^+$ primary ion gun in the static mode (primary ion dose of about$\cdot 3\bullet 10^{10}$ ions $cm^{-2}$). The analyzed area corresponds to a square of 500 μm × 500 μm. For each sample, three spectra from different areas of the surface were analyzed. Before the measurements, the samples were pressed into pellets and attached to the sample holder with double-sided tape. A pulsed electron flood gun was used for charge compensation.

*2.2.6. XPS*

X-ray Photoelectron Spectroscopy spectra of the main core levels were carried out using a multi-chamber ultra-high vacuum (UHV) system equipped with SES R4000 hemispherical analyzer (Gammadata Scienta). The elemental composition of the surface and identification of the chemical bonds present on the zeolite surface were obtained from spectra recorded at room temperature and under UHV conditions ($2 \times 10^{-9}$ mbar). Non-monochromatic radiation $AlK_{\alpha}$ (1486.6 eV) was used to generate electron excitations from the core. Calibration of the spectrometer was carried out in accordance with ISO 15472:2001. The energy resolution of the system operating at a fixed pass energy of 100 eV was 0.9 eV (measured as the full width at half maximum for the Ag $3d_{5/2}$ core line). The binding energy (BE) of the adventitious carbon species (C 1 s line at BE = 285.0 eV) was used to correct the measured spectra for surface charging. Quantitative analysis was performed in CasaXPS 2.3.23 software after subtracting the Shirley-type background and fitting the experimental spectra with a pseudo-Voigt line shape (a combination of Gaussian and Lorentzian functions in a 30:70 ratio).

*2.2.7. Mössbauer spectroscopy*

$^{57}$Fe Mössbauer studies were performed in transmission geometry using a conventional constant-acceleration spectrometer (Science Engineering & Education Co. USA) with top loaded liquid helium cryostat (Janis Research Company, Wilmington, MA 01887, USA). $^{57}$Co(Rh) γ-ray source and absorbers made of finely powdered zeolites placed in thin-walled cylindrical plastic containers were kept at room temperature. Optimization of absorber thickness of about 80–130 mg cm$^{-2}$ was made according to the procedure proposed by Long et al. [13]. The detection of resonance 14.4 keV γ-rays and the calibration of the drive velocity were performed simultaneously using two independent Kr/$CO_2$ proportional gas counters (LND, Inc. Oceanside, NY, USA) placed at opposite sides of the driving system. Mössbauer spectra were analyzed in Recoil 1.05 software using the hyperfine parameter distributions based on Rancourt and Ping method [14]. In this approach, the distribution of hyperfine parameters for a particular crystal site corresponding to similar structural, chemical and magnetic properties is constructed by the sum of Voigt components for the quadrupole splitting (QS) distributions and, if necessary, the magnetic hyperfine field distributions.

*2.2.8. TGA-DTA-MS*

Thermogravimetry – Differential Thermal Analysis – Mass Spectrometry (TGA-DTA-MS) analysis including thermogravimetric (TG) and differential thermal analysis (DTA) and mass spectrometry (MS) has been performed using a SETSYS 16/18 derivatograph, Setaram (France) and a ThermoStar mass spectrometer, Balzers (Germany). TGA-DTA and MS spectra were recorded in air flow (Air Liquide, 99.99% of purity, 40 cm$^3$ min$^{-1}$) for a temperature range of 0–900 °C with a heating rate of 10 °C min$^{-1}$. Sample masses ranged from 10 to 20 mg, and samples were weighted in the corundum crucible. These studies were used to describe the amount and type of coke deposition. Temperature-programmed oxidation was carried out under conditions stated above and a mass spectrometer was used as a detector of $CO_2$ formation, and the amount of oxidized carbon was measured with a TGA detector. DTA analysis provided additional information on thermal effects during TPO.

*2.2.9. Catalytic tests*

FTS catalytic tests were carried out in a steel fixed bed microreactor (length 48 cm, internal dimeter 6 mm, wall thickness 2 mm) using a gas mixture of $H_2$ and CO with a molar ratio 2:1 and a total reactant flow rate of 60 mL · min$^{-1}$ (measured under standard, RT and 1 atm conditions and also controlled during the reaction). The mass of powdered catalyst samples was 500 mg, the height of the catalyst bed was 7 mm, and the approximate GHSV was 2962.5 h$^{-1}$. The reaction was carried out at a pressure of 30 atm at 300 °C, and the gaseous reactants were analyzed using a gas chromatograph (Shimadzu GC – 14) equipped with a TCD detector and two columns: measurement column – Carbosphere 7 A and comparison column – molecular sieves 7B. GC measurements parameters: column temperature – 45 °C, detector temperature – 120 °C, detector current – 100 mA; carried gas – 8% $H_2$–92% He (Air Liquide, 99.999% of purity). Prior to the FT reaction, the catalysts were reduced *in situ* under atmospheric pressure in a flow of 95% $H_2$–5% Ar gas mixture (Air Liquide, 99.999% of purity) at 400 °C for 1 h.

During the reaction, the liquid products formed were directed to a cooler connected to the reactor, cooled and collected in a special tank. The liquid products were analyzed by GC–MS coupled technique. A gas chromatograph equipped with a Zebron Phase ZB-1MS capillary column (6890 N Network GC System) was coupled to a quadrupole mass spectrometer (5973 Network Mass Selective Detector) with an autosampler (7683 Series Injector). The column length was 30 m and the internal diameter was 0.25 mm. The liquid products, in order to remove any water that may have formed during the reaction, were concentrated by SPE method on C18 octadecyl columns. Before extraction, each column was preconditioned with 2 mL of n – hexane. After this process, a 1 mL sample of liquid products was injected onto the column and washed with 2 mL of n – hexane. GC – MS analysis were carried out in helium flow (0.7 mL · min$^{-1}$) in the temperature range of 60–280 °C with a linear temperature increase of 10 °C min$^{-1}$. The volume of analyzed sample was 1 mm$^3$.

The quantitative analysis of CO conversion ($X_{CO}$) and selectivity towards $CO_2$ ($S_{CO2}$), $C_1$ – $C_4$ gaseous hydrocarbons (labelled as $S_{C1\text{-}C4}$;) and liquid products – hydrocarbons $C_{5+}$ ($S_{LP}$) were calculated as follows:

$$\mathbf{X_{CO}} = \frac{\mathbf{A_{COin} - A_{COari}}}{\mathbf{A_{COin}}} * \mathbf{100\%}$$

$$\mathbf{S_{C_1-C_4}} = \frac{\mathbf{A_{C_1-C_4i}} * \mathbf{100\%}}{\mathbf{A_{CH_4out}}} \Big/ \mathbf{F}$$

$$\mathbf{A_{C_1-C_4out}} = \frac{\mathbf{A_{C_1-C_4s}} * \mathbf{X_{CO}}}{\mathbf{100\%}}$$

$$\mathbf{S_{CO_2}} = \frac{\mathbf{A_{CO_2i}} * \mathbf{100\%}}{\mathbf{A_{CO_2out}}} \Big/ \mathbf{F}$$

$$\mathbf{A_{CO_2out}} = \frac{\mathbf{A_{CO_2s}} * \mathbf{X_{CO}}}{\mathbf{100\%}}$$

where:

$X_{CO}$ – CO conversion.

$A_{COin}$ – CO peak area at the inlet before the reaction (standard).

$A_{COari}$ – CO peak area after the reaction.

$S_{C1\text{-}C4}$ – selectivity towards gaseous hydrocarbons $C_1$ – $C_4$.

$S_{CO2}$ – selectivity towards $CO_2$.

$A_{C1\text{-}C4i}$ – $C_1$-$C_4$ peak area formed during the reaction.

$A_{CO2i}$ – $CO_2$ peak area formed during the reaction.

$A_{C1\text{-}C4out}$ – the area of the theoretical $C_1$-$C_4$ peak which could be formed during the reaction if all the CO was converted to $C_1$-$C_4$ gaseous hydrocarbons.

$A_{CO2out}$ – the area of the theoretical $CO_2$ peak which could be formed during the reaction if all CO is converted to $CO_2$.

$A_{CH4s}$ –$CH_4$ standard peak area when only methane is analyzed.

$A_{CO2s}$ –$CO_2$ standard peak area when only carbon dioxide is analyzed.

F – contraction coefficient to account for flow changes and differences between gaseous substrates and liquid products:

$$\mathbf{F} = \frac{\mathbf{A_{Ar\ i}}}{\mathbf{S_{Ar\ s}}}$$

$A_{Ar\ i}$ —Ar (inert gas) peak area during reaction.

$A_{Ar\ s}$ —Ar peak area at the inlet before reaction (standard).

Selectivity to liquid products (all liquid products formed) was calculated based on the following equation:

$$\mathbf{S_{LP} = 100 - (S_{C1\text{-}C4} + S_{CO2}).}$$

The Anderson-Schultz-Flory distribution of the obtained products was estimated to determine the probability of chain growth (α). We assumed that α is independent of the hydrocarbon chain length, and in this case the Anderson-Schultz-Flory equation can be represented as follows:

$$log(W_n/n) = n\log\alpha + const$$

where: $W_n$ is the mass fraction of the species with the number of carbon atoms n. From the slope of the plot of $\log(W_n/n)$ against n, the value of α was obtained.

## 3. Results

### 3.1. Textural and structural characterization and phase composition (BET, XRD)

The BET surface area with micropore area and external surface area, total pore volume, micropore volume and average pore size of calcined bimetallic iron-cobalt BEA zeolite catalysts are summarized in Table 1. The $N_2$ adsorption-desorption isotherms of these two catalyst series are shown in Supplementary Information (Fig. S1(a) – S1(c) for C-FeCoAlBEA and Fig. S1(d) – S1(f) for C-FeCoSiBEA). All $N_2$ adsorption-desorption isotherms show a typical type I isotherm with a substantial hysteresis loop H4 from $P/P_0 = 0.45$ with a characteristic step-down in the desorption branch associated with the hysteresis loop closure according to the IUPAC classification [15]. Such course of isotherms indicates a micro-*meso* hierarchical porous textural feature.

For C- $Fe_xCo_y$AlBEA samples, a decrease in specific surface area was observed after the addition of metals compared to pure AlBEA zeolite (610 $m^2/g$) [16]. The SSA for C—$Fe_{2.5}Co_{2.5}$AlBEA was 464 $m^2/g$, for C—$Fe_{5.0}Co_{5.0}$AlBEA – 421 $m^2/g$ and decreases significantly for the sample with the highest amount of metals to 383 $m^2/g$, while a decrease in total pore volume was observed. The volume of micropores for all $Fe_xCo_y$AlBEA catalysts was similar, and the average pore radius decreased slightly, which can suggest that some metal species or ions are localized inside the pores of the AlBEA zeolite. A similar relationship was observed for mono- and bimetallic cobalt-iron catalysts supported on SBA-15 [2].

In the case of C-$Fe_xCo_y$SiBEA, the decrease in specific surface area was greater than for non-dealuminated samples, and a significant decrease to 104 $m^2/g$ was found for the sample with the highest metal loading. For these catalysts, a decrease in the volume of micropores was observed from 0.17 $cm^3/g$ to 0.03 $cm^3/g$ for C-$Fe_{10}Co_{10}$SiBEA sample. The average pore radius for C—$Fe_{2.5}Co_{2.5}$SiBEA was 7.07 nm, decreasing slightly for the sample with 5 wt% metal loading to 6.65 nm and increasing almost 2-fold for the sample with the highest amount of metals to 13.7 nm. A similar effect was observed for bimetallic cobalt-iron supported on HMS by Bragança et al. [2]. The shape of the pore distribution curves is shown in the Supplementary Information (Fig. S2)

Fig. 1 presents the XRD patterns of the catalysts C-$Fe_xCo_y$AlBEA (Fig. 1a) and

C-$Fe_xCo_y$SiBEA (Fig. 1b) prepared by sequential wet impregnation. For both series, characteristic 2θ peaks of about 22.4°, typical of BEA materials, were observed, in accordance with previous reports [–,9,16,18]. The position of the main diffraction reflex for C-FeCoSiBEA samples (2θ = 22.60°) is slightly shifted compared to C-FeCoAlBEA samples (2θ = 22.47°). However, the observed changes are very small and may indicate a slight shrinkage of the matrix during HAlBEA dealumination and expansion after the introduction of metal ions into the SiBEA structure.

In the case of C-$Fe_xCo_y$AlBEA catalysts, peaks attributed to $Fe_2O_3$ and $Co_3O_4$ species were observed (Fig. 1a). It is worth mentioning that for the C—$Fe_{2.5}Co_{2.5}$AlBEA sample, a predominantly $Fe_2O_3$ phase (85%; Table 2) was observed, which can suggest that cobalt ions are mainly localized in the ion-exchange positions of the BEA zeolite. The content of $Co_3O_4$ phase increases with increasing cobalt ion loading, and for C-$Fe_{10}Co_{10}$AlBEA the percentage of this phase is 40%, and that of the $Fe_2O_3$ phase is 50% (Table 2).

Peaks attributed to $Fe_2O_3$, $Fe_3O_4$ and $Co_3O_4$ are observed in C—$Fe_{2.5}Co_{2.5}$SiBEA and C—$Fe_{5.0}Co_{5.0}$SiBEA samples (Fig. 1b). It should be mentioned that the $Fe_3O_4$ (magnetite) phase is dominant (Table 2), which may affect the reducibility of these catalysts. In addition, the small percentage of $Co_3O_4$ phase may mean that cobalt ions react with the silanol groups of vacant T-atom sites with their incorporation into the framework of zeolite, thus creating new catalytic properties. For the sample with the highest metal loading, only the $Fe_2O_3$ and $Co_3O_4$ phases are observed, with the cobalt phase being dominant (Table 2). It is very likely that these high metal loads and more cobalt and iron oxides are localized on the external surface of the BEA zeolite and cover other metal species, but it is not excluded that cobalt ions are also localized in the framework of the BEA zeolite.

To determine the nature of cobalt and iron ions present in the C-$Fe_xCo_y$AlBEA and C-$Fe_xCo_y$SiBEA samples, a time-of-flight secondary ion mass spectrometry (ToF-SIMS) analysis was performed. The results of the ToF-SIMS measurement are summarized in Table 3. ToF-SIMS is a surface-based technique, and the difference between detected ions can be significant because their concentrations on the surface vary. However, based on the normalized ion intensities, it is possible to determine surface ions connections and gain additional knowledge about the nature of cobalt and iron species in SiBEA and AlBEA zeolites. Analysis of C—$Fe_{2.5}Co_{2.5}$AlBEA and C-$Fe_{10}Co_{10}$AlBEA samples showed the presence of $CoAlO^+$, $CoAlO_2H^+$, $CoSiOH^+$, $CoSiO_2H^+$, $FeAlO^+$, $FeAlO_2H^+$, $FeSiOH^+$ ions, which confirmed the formation of aluminates or aluminosilicates and silicates of cobalt and iron and may indicate the localization of these metals in ion-exchange or framework positions and their strong interaction with the AlBEA zeolite support.

For the dealuminated C—$Fe_{2.5}Co_{2.5}$SiBEA and C-$Fe_{10}Co_{10}$SiBEA samples, only $CoSiOH^+$, $CoSiO_2H^+$, $FeSiOH^+$ ions were detected, and their normalized intensities were higher than those calculated for the non-dealuminated samples, which may suggest that cobalt and iron silicates are formed and the ions are localized in the framework positions of the SiBEA zeolite. It should also be noted that the calculated $Al^+$ ion intensities for the dealuminated samples are much lower than those for the non-dealuminated catalysts, and the $Al^+/Si^+$ ratio is also lower, which clearly proves that the dealumination process occurring in the first step of the preparation of C-$Fe_xCo_y$SiBEA samples (where x = 2.5; 5.0 and 10 wt% of Fe and y = 2.5; 5.0 and 10 wt% of Co) was successful.

Moreover, $Fe^+$ and $Co^+$ ions were also found on the surface of all studied samples, which can be proved in connection with XRD analysis

**Table 1**
Textural properties of bimetallic $Fe_xCo_y$SiBEA and $Fe_xCo_y$AlBEA catalysts after calcination at 500 °C for 3 h.

| Sample | SSA (BET) ($m^2/g$) | Total pore volume (BJH) ($cm^3/g$) | Micropore volume ($cm^3/g$) | Micropore Area ($m^2/g$) | External Surface ($m^2/g$) | Average pore radius (BJH) (nm) |
|---|---|---|---|---|---|---|
| $Fe_{2.5}Co_{2.5}$SiBEA | 463 | 0.48 | 0.17 | 329 | 134 | 7.1 |
| $Fe_{2.5}Co_{2.5}$AlBEA | 464 | 0.51 | 0.16 | 316 | 148 | 6.9 |
| $Fe_{5.0}Co_{5.0}$SiBEA | 423 | 0.43 | 0.15 | 290 | 133 | 6.7 |
| $Fe_{5.0}Co_{5.0}$AlBEA | 421 | 0.46 | 0.15 | 284 | 138 | 6.5 |
| $Fe_{10}Co_{10}$SiBEA | 104 | 0.28 | 0.03 | 64 | 40 | 13.7 |
| $Fe_{10}Co_{10}$AlBEA | 383 | 0.38 | 0.13 | 258 | 125 | 5.8 |

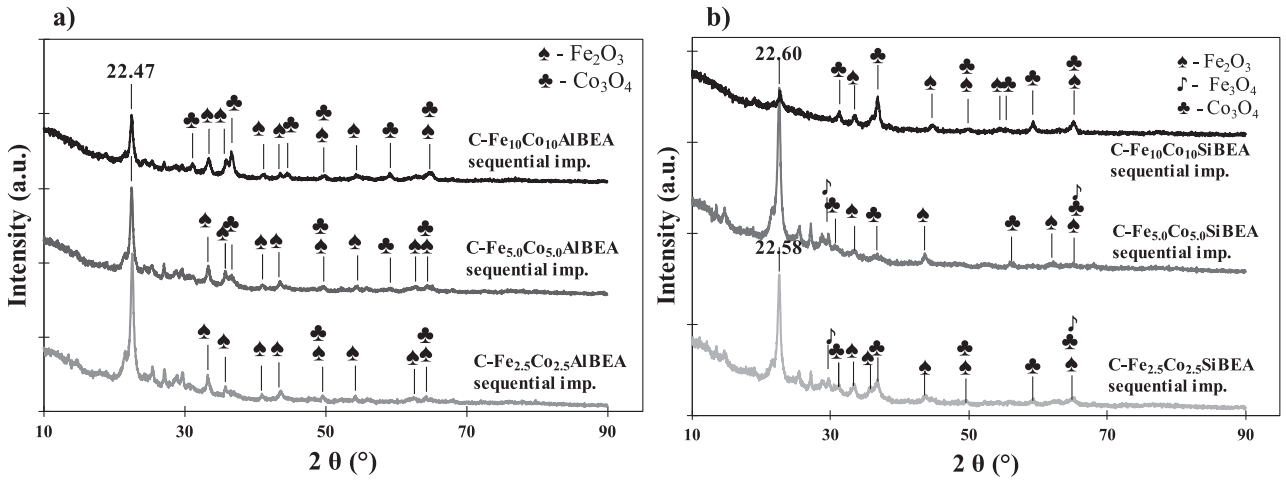


**Fig. 1.** XRD patterns of C-$Fe_xCo_y$AlBEA (a) and C-$Fe_xCo_y$SiBEA (b) catalysts after calcination at 500 °C for 3 h.

**Table 2**
Phase composition of bimetallic $Fe_xCo_y$SiBEA and $Fe_xCo_y$AlBEA catalysts after calcination at 500 °C for 3 h calculated from XRD data.

| Sample | $Fe_2O_3$ (wt%) | $Co_3O_4$ (wt%) | $Fe_3O_4$ (wt%) |
|---|---|---|---|
| $Fe_{2.5}Co_{2.5}$SiBEA | 23 | 27 | 50 |
| $Fe_{2.5}Co_{2.5}$AlBEA | 85 | 15 | – |
| $Fe_{5.0}Co_{5.0}$SiBEA | 11 | 10 | 79 |
| $Fe_{5.0}Co_{5.0}$AlBEA | 65 | 35 | – |
| $Fe_{10}Co_{10}$SiBEA | 29 | 71 | – |
| $Fe_{10}Co_{10}$AlBEA | 50 | 40 | – |

that metals oxides form in extra-framework positions and inside the channels of BEA zeolites. The calculated $Fe^+/Co^+$ ion ratio could suggests that for the samples with the highest metal loading, iron oxides are dominant and cobalt ions are partially localized in the BEA zeolite structure. In addition, the normalized $Co^+$ ion intensities for the C-$Fe_xCo_y$SiBEA samples, are much lower than those for the C-$Fe_xCo_y$AlBEA samples, indicating that cobalt is mainly present in the SiBEA zeolite at the framework positions in the vacant T-atom sites formed, and only an excess amount of cobalt is present at extra-framework positions. These results are consistent with XRD analysis and prove that the two step post-synthesis method allows the controlled incorporation of metal ions into the structure of the BEA zeolite and the formation of new active sites and the design of catalysts with unique new catalytic properties.

### 3.2. Reducibility (TPR-$H_2$, XRD and ToF-SIMS)

The reduction of cobalt and iron oxides is always a multi-step process. The reduction of cobalt oxides in $H_2$ occurs in two steps according to the equations:

$$Co_3O_4 + H_2 \rightarrow 3CoO + H_2O$$

$$CoO + H_2 \rightarrow Co^0 + H_2O$$

These two steps are usually clearly visible for $Co_3O_4$ in bulk form and in monometallic catalysts [3]. However, it should be mentioned that the reduction of cobalt species in monometallic cobalt BEA zeolite catalysts was described in our earlier work [9,17]. This process proceeds in four steps due to the presence of not only cobalt oxides, but also other cobalt species, such as octahedral Co (II) species well dispersed in the BEA structure and isolated pseudo-tetrahedral Co (II) species localized in the framework of the BEA zeolite.

Similarly, the reduction of pure $Fe_2O_3$ in $H_2$ takes place in two or three steps according to the equations below and depends on the temperature used for this process and the rate of temperature rise during TPR measurements [3,19,20]:

$$3Fe_2O_3 + H_2 \rightarrow 2Fe_3O_4 + H_2O.$$

$$Fe_3O_4 + 4H_2 \rightarrow 3Fe + 4H_2O$$

or

$$3Fe_2O_3 + H_2 \rightarrow 2Fe_3O_4 + H_2O$$

**Table 3**
The normalized intensities of secondary ions calculated using ToF-SIMS data obtained for FeCoSiBEA and FeCoAlBEA catalysts after calcination at 500 °C for 3 h.

| | Samples | | | |
|---|---|---|---|---|
| Ions | C-$Fe_{2.5}Co_{2.5}$SiBEA | C-$Fe_{10}Co_{10}$SiBEA | C-$Fe_{2.5}Co_{2.5}$AlBEA | C-$Fe_{10}Co_{10}$AlBEA |
| | The Normalized Ions Intensities | | | |
| $Al^+$ | $1.1 \times 10^{-3}$ | $1.0 \times 10^{-3}$ | $28.4 \times 10^{-3}$ | $25.4 \times 10^{-3}$ |
| $Si^+$ | $97 \times 10^{-3}$ | $44 \times 10^{-3}$ | $150 \times 10^{-3}$ | $119 \times 10^{-3}$ |
| $Fe^+$ | $5.6 \times 10^{-3}$ | $9.1 \times 10^{-3}$ | $2.6 \times 10^{-3}$ | $18.3 \times 10^{-3}$ |
| $Co^+$ | $23.1 \times 10^{-3}$ | $4.3 \times 10^{-3}$ | $7.2 \times 10^{-3}$ | $10.0 \times 10^{-3}$ |
| $Fe^+/Co^+$ | 0.24 | 2.10 | 0.36 | 1.82 |
| $Al^+/Si^+$ | 0.012 | 0.023 | 0.189 | 0.213 |
| $CoAlO^+$ | – | – | $2.1 \times 10^{-4}$ | $4.0 \times 10^{-4}$ |
| $CoAlO_2H^+$ | – | – | $0.6 \times 10^{-4}$ | $0.9 \times 10^{-4}$ |
| $CoSiOH^+$ | $8.7 \times 10^{-4}$ | $3.3 \times 10^{-4}$ | $1.9 \times 10^{-4}$ | $2.8 \times 10^{-4}$ |
| $CoSiO_2H^+$ | $3.5 \times 10^{-4}$ | $1.0 \times 10^{-4}$ | $1.1 \times 10^{-4}$ | $1.1 \times 10^{-4}$ |
| $FeAlO^+$ | – | – | $1.0 \times 10^{-4}$ | $2.2 \times 10^{-4}$ |
| $FeAlO_2H^+$ | – | – | $0.8 \times 10^{-4}$ | $1.2 \times 10^{-4}$ |
| $FeSiOH^+$ | $7.4 \times 10^{-4}$ | $3.0 \times 10^{-4}$ | $1.2 \times 10^{-4}$ | $2.3 \times 10^{-4}$ |

$2Fe_3O_4 + 2H_2 \rightarrow 6FeO + 2H_2O$

$6FeO + 6H_2 \rightarrow 6Fe + 6H_2O$

The mechanism of iron oxides reduction strongly depends on the experimental conditions. A three step reduction process was observed when the $X_{H2O}/X_{H2}$ ratio was high and a two-step reduction process when the ratio was low [20].

According to our previous work, the reduction of iron species present in monometallic FeSiBEA catalysts is multistep (four reduction steps was observed) and indicates the presence of different types of iron species in this catalytic system [10]. This means that the reduction of metal species present in different catalytic systems is more complicated and sometimes difficult to identify all species and interpret. This sometimes requires various techniques that can help to determine the reducibility of metals species.

Fig. 2 presents the TPR profiles obtained for the catalysts C-$Fe_xCo_y$AlBEA (Fig. 2a) and C-$Fe_xCo_y$SiBEA (Fig. 2b). Fig. S3 in Supplementary Information shows the TPR patterns for C—$Fe_{2.5}Co_{2.5}$AlBEA (Fig. S3a) and C—$Fe_{2.5}Co_{2.5}$SiBEA (Fig. S3b) catalysts in order to better visualize all the reduction peaks. Several reduction peaks were observed for both series. The course of the TPR profiles for these two catalyst series is different, suggesting that different types of metal species are present in these two catalyst series.

In the case of the non-dealuminated series of C-$Fe_xCo_y$AlBEA catalyst, two reduction peaks were observed for the C—$Fe_{2.5}Co_{2.5}$AlBEA sample (Fig. 2a and Fig. S3a) or three reduction peaks for the C—$Fe_{5.0}Co_{5.0}$AlBEA and C-$Fe_{10}Co_{10}$AlBEA samples. Based on the XRD results, the present phase in these catalysts is mainly $Fe_2O_3$ and a smaller amount of $Co_3O_4$. For the C—$Fe_{2.5}Co_{2.5}$AlBEA sample two regions of reduction were noticed, the first in temperature range of 220–530 °C with a maximum at 390 °C, which can be assigned to the reduction of mainly iron oxides to metallic iron and probably a partial reduction of $Co_3O_4$, the second small broad peak in the temperature range of 530–790 °C with a maximum at 680 °C can be described as the reduction of metals ions more strongly bound to supports such as aluminosilicates or present in the ion-exchange positions, which is consistent with the ToF-SIMS results (Table 3, analyzed above and Table 4) and the XRD results. This broad peak could also be the result of interactions between cobalt and iron and the formation of a new phase of mixed Co—Fe oxides [21].

For the catalysts C—$Fe_{5.0}Co_{5.0}$AlBEA and C-$Fe_{10}Co_{10}$AlBEA, a slightly different course of TPR profiles was observed, probably related to the increase in the percentage of the $Co_3O_4$ phase in these samples (Table 2). Three regions of reduction were found for these catalysts, the first in the lower temperature range of 260–320 °C with maximum at 290 and 310 °C for the catalysts C—$Fe_{5.0}Co_{5.0}$AlBEA and C-$Fe_{10}Co_{10}$AlBEA, respectively, which can be assigned to the first step of reduction of the iron and cobalt oxides $Fe_2O_3$ and $Co_3O_4$, which is consistent with our earlier reports for the monometallic zeolite catalysts C-CoBEA and C-FeBEA, for which we observed a similar range of reduction temperatures for these metal oxides [9,10,16]. The second peak in the temperature range of 310–390 °C with maxima at 330 and 360 °C, respectively, is probably related to the further simultaneous reduction of $Fe_3O_4$ or FeO to metallic iron and CoO to metallic cobalt. A third reduction peak registered in the temperature range of 360–550 °C with a maximum at 420 °C for C—$Fe_{5.0}Co_{5.0}$AlBEA and 440 °C for C-$Fe_{10}Co_{10}$AlBEA, which may be related to the reduction of metal ions in the ion-exchange positions or aluminosilicates of cobalt and iron. However, it is worth mentioning that the XRD results shown in Fig. 3 obtained for the C—$Fe_{5.0}Co_{5.0}$AlBEA sample after reduction in hydrogen flow for 1 h at 400 °C indicate that after reduction under such conditions, metallic iron and the $Co_3O_4$ phase are the main phases in the catalysts studied. In addition, ToF-SIMS measurements performed for this sample after reduction at 400 °C indicate the presence of iron and cobalt aluminosilicates, proving that the third reduction region identified on the TPR profiles is related to reduction of metal species strongly associated with the AlBEA zeolite support (Table 4).

In the case of the C-$Fe_xCo_y$SiBEA series of catalysts (Fig. 2b), the reduction process is also multi-step, and the reduction maxima are slightly shifted at a higher temperature compared to the C-$Fe_xCo_y$AlBEA samples. Four reduction peaks were observed for the C—$Fe_{2.5}Co_{2.5}$SiBEA (Fig. 2b and Fig. S3b) and C—$Fe_{5.0}Co_{5.0}$SiBEA (Fig. 2b) samples, and five reduction peaks were found for the C-$Fe_{10}Co_{10}$SiBEA sample (Fig. 2b). According to the XRD results (Fig. 1), the main phase in the C—$Fe_{2.5}Co_{2.5}$SiBEA and C—$Fe_{5.0}Co_{5.0}$SiBEA catalysts was $Fe_3O_4$, with

**Table 4**
The normalized intensities of secondary ions calculated using ToF-SIMS data obtained for FeCoSiBEA and FeCoAlBEA catalysts after calcination at 500 °C for 3 h and reduction at 400 °C for 1 h.

| Ions | Samples | | |
|---|---|---|---|
| | Red-C-$Fe_{2.5}Co_{2.5}$SiBEA | Red-C-$Fe_{5.0}Co_{5.0}$SiBEA | Red-C-$Fe_{5.0}Co_{5.0}$AlBEA |
| | The Normalized Ions Intensities | | |
| $Al^+$ | $3.5 \times 10^{-3}$ | $3.9 \times 10^{-3}$ | $26.7 \times 10^{-3}$ |
| $Si^+$ | $240 \times 10^{-3}$ | $167 \times 10^{-3}$ | $104 \times 10^{-3}$ |
| $Fe^+$ | $11.6 \times 10^{-3}$ | $13.2 \times 10^{-3}$ | $6.0 \times 10^{-3}$ |
| $Co^+$ | $14.8 \times 10^{-3}$ | $15.8 \times 10^{-3}$ | $21.6 \times 10^{-3}$ |
| $Fe^+/Co^+$ | 0,78 | 0,83 | 0,28 |
| $Al^+/Si^+$ | 0,015 | 0,024 | 0,257 |
| $CoAlO^+$ | x | x | $4.3 \times 10^{-4}$ |
| $CoAlO_2H^+$ | x | x | $1.0 \times 10^{-4}$ |
| $CoSiOH^+$ | $1.5 \times 10^{-4}$ | $1.9 \times 10^{-4}$ | $3.3 \times 10^{-4}$ |
| $CoSiO_2H^+$ | $1.2 \times 10^{-4}$ | $1.2 \times 10^{-4}$ | $2.1 \times 10^{-4}$ |
| $FeAlO^+$ | x | x | $2.0 \times 10^{-4}$ |
| $FeAlO_2H^+$ | x | x | $1.3 \times 10^{-4}$ |
| $FeSiOH^+$ | $1.1 \times 10^{-4}$ | $1.6 \times 10^{-4}$ | $2.4 \times 10^{-4}$ |

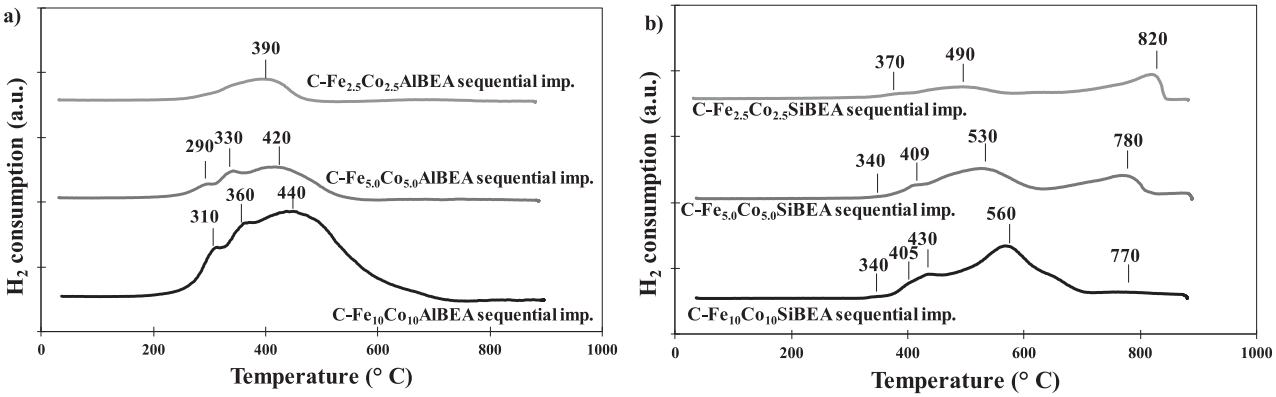


**Fig. 2.** TPR profiles of a). C-$Fe_xCo_y$AlBEA (a) and C-$Fe_xCo_y$SiBEA (b) catalysts after calcination at 500 °C for 3 h.

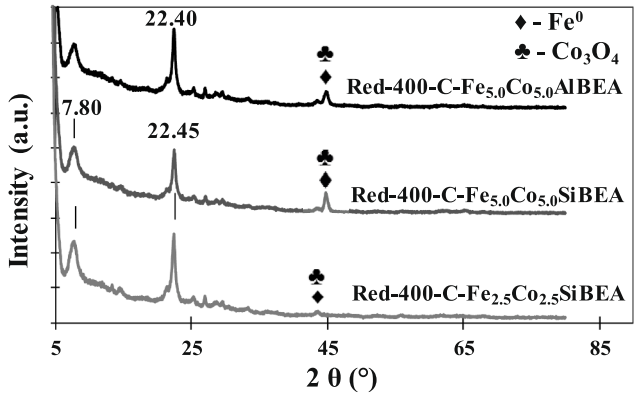


**Fig. 3.** XRD patterns of Red-400-C-$Fe_{2.5}Co_{2.5}$SiBEA, Red-400-C-$Fe_{5.0}Co_{5.0}$SiBEA and Red-400-C-$Fe_{5.0}Co_{5.0}$AlBEA catalysts after their activation at 400 °C for 1 h in hydrogen flow. (For interpretation of the references to colour in this figure legend, the reader is referred to the web version of this article.)

$Fe_2O_3$ and $Co_3O_4$ in smaller amounts, which may affect the nature of the reduction of these samples. For these samples, the first very small reduction peak was detected in the temperature range of 320–390 °C with a maximum at 370 °C for C—$Fe_{2.5}Co_{2.5}$SiBEA and 340 °C for C—$Fe_{5.0}Co_{5.0}$SiBEA and C-$Fe_{10}Co_{10}$SiBEA, which can be assigned to the simultaneous reduction of iron oxides ($Fe_2O_3$ to $Fe_3O_4$ or $Fe_3O_4$ to FeO) and cobalt oxides ($Co_3O_4$ to CoO). A second higher and broader reduction peak in the temperature range of 410–580 °C with a maximum at 490 °C observed for C—$Fe_{2.5}Co_{2.5}$SiBEA; 390–430 °C with a maximum at 409 °C found for C—$Fe_{5.0}Co_{5.0}$SiBEA and two peaks, the second in the temperature range of 370–420 °C with a maximum at 405 °C and the third in the temperature range of 420–470 °C with a maximum at 430 °C noted for C-$Fe_{10}Co_{10}$SiBEA are probably related to further reduction of iron and cobalt oxides to metallic iron and cobalt. The XRD results obtained for C—$Fe_{2.5}Co_{2.5}$SiBEA and C—$Fe_{5.0}Co_{5.0}$SiBEA after reduction in hydrogen flow for 1 h at 400 °C (Fig. 3) suggests that the first and second reduction peaks in the TPR profiles are mainly related to the reduction of $Fe_3O_4$ and $Fe_2O_3$ phases, as XRD mainly indicates the presence of metallic iron and $Co_3O_4$ after reduction under such conditions (Fig. 3). The third or fourth (for samples with the highest metal loading) reduction peak was observed in the temperature range of 430–680 °C with a maximum at 630 °C for C—$Fe_{2.5}Co_{2.5}$SiBEA, 530 °C for C—$Fe_{5.0}Co_{5.0}$SiBEA and 560 °C for C-$Fe_{10}Co_{10}$SiBEA, which can be attributed to the reduction of octahedral Co (II) species or the reduction of cobalt silicates. The final high and narrow reduction peak in the temperature range of 670–850 °C with a maximum at 820 °C for C—$Fe_{2.5}Co_{2.5}$SiBEA, 780 °C for C—$Fe_{5.0}Co_{5.0}$SiBEA and 770 °C for C-$Fe_{10}Co_{10}$SiBEA can be ascribed as the reduction of isolated pseudo-tetrahedral cobalt species present in the framework of the BEA zeolite, which is consistent with our previous work [9,16].

### 3.3. Spectroscopic characterization (Mössbauer Spectroscopy and XPS)

$^{57}$Fe Mössbauer spectroscopy was used to study the oxidation state of iron introduced into the zeolite structure, as well as to determine the local coordination environment of various iron species, which consequently allowed the identification of intra- and extra-framework species. The room temperature $^{57}$Fe Mössbauer spectra for selected zeolites are presented in Fig. 4. As one can see all spectra consist of a superposition of magnetic sextets and non-magnetic doublets. To drew attention, the components originating from magnetic iron oxides have been filled in black, while the non-magnetic components have been filled in light grey. It is worth mentioning, that the magnetic components must origin from iron oxides having a critical temperature (Curie $T_C$ or Néel $T_N$) higher than the room temperature at which the measurements were made. The best candidates here are hematite α-$Fe_2O_3$ (948 K), maghemite γ-$Fe_2O_3$

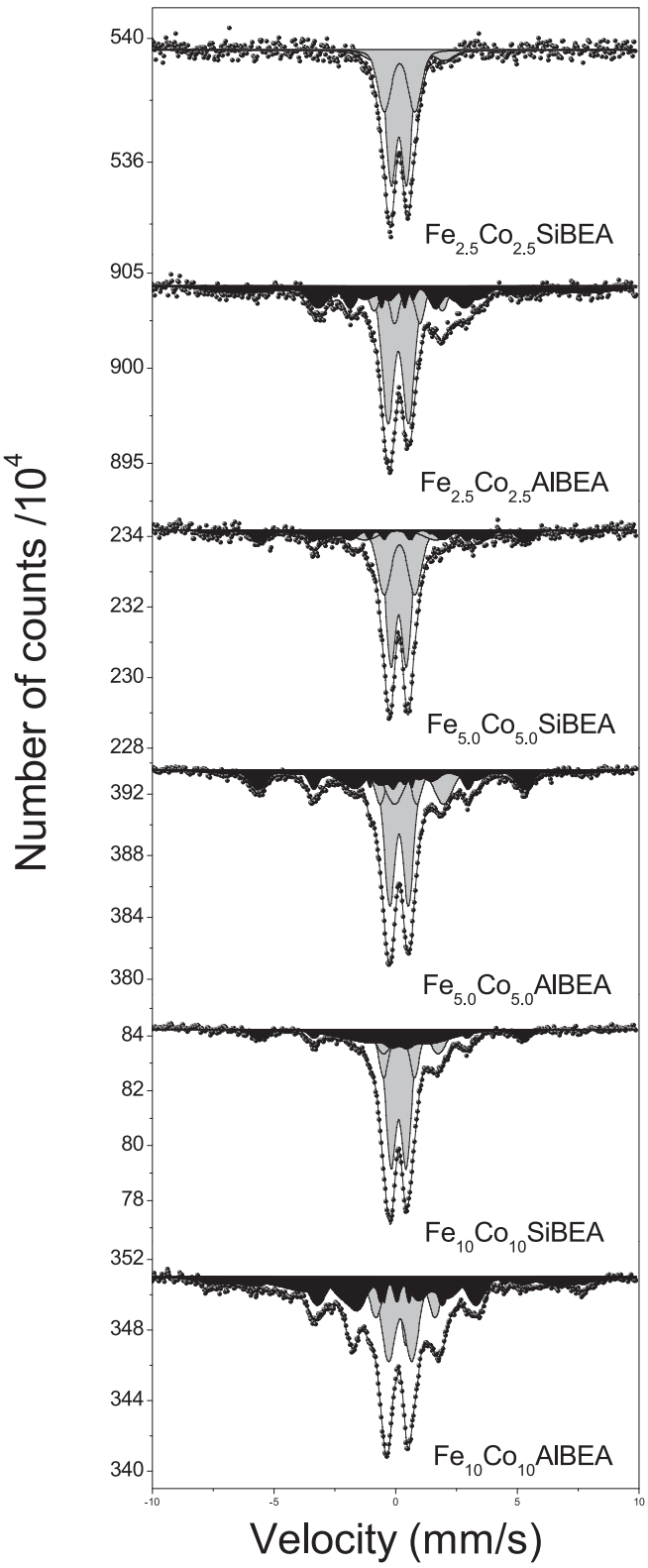


**Fig. 4.** Room temperature $^{57}$Fe Mössbauer spectra and their deconvolution for the $Fe_xCo_y$SiBEA and $Fe_xCo_y$AlBEA zeolites. The light grey components are related to the non-magnetic iron species. The black components correspond to magnetic species.

(833 K), magnetite $Fe_3O_4$ (858 K) and cobalt spinel ferrite $CoFe_2O_4$ (793 K). Unambiguous identification of magnetic phases is impossible due to lack of well-defined magnetic sextets. This is a common case when the relaxation phenomena related to the existence of ultrafine particles of $Fe_2O_3$ and/or other iron oxide phases of superparamagnetic character cause the magnetic hyperfine field is much lower than existing in bulk $Fe_2O_3$ [22,23]. In such case the sharp magnetic sextets collapse into asymmetrically broadened lines making it impossible to clearly identify individual components. However, also taking into account the XRD results, it can be concluded that some extra-framework species seen in studied zeolites are most probably $Fe_2O_3$ and $Fe_3O_4$ nanoparticles.

In the central part of all spectra there is an asymmetric doublet which can be fitted by three symmetric quadrupole doublets according to the numerical procedure described above. The corresponding hyperfine parameters such as electric quadrupole splitting (QS), isomer shift (IS), width of the quadrupole splitting distribution (σ) and the resonance area (A) in percent of the total iron are summarized in Table 5. Low value of isomer shift (IS <0.3 mm/s) is typical for the high spin $Fe^{3+}$ ions in a tetrahedral oxygen coordination [24 – 26], which confirms the incorporation of $Fe^{3+}$ ions in the framework of zeolite. The presence of two quadrupole doublets with similar IS and different QS can be explained according to the non-equivalent surface and bulk Fe atoms in core-shell model [27]. The doublet with lowest QS = 0.63–0.84 mm/s belongs to iron species located in the well-defined framework sites with high symmetry, and therefore those coming from the core of the particles. The second doublet with larger QS = 0.96–1.50 mm/s can be assigned to the surface ferric ions such as $(SiO)_2$-$Fe^{3+}$-O-$Fe^{3+}$-(OH)(OSi) [28]. The high values of the quadrupole splitting parameter reflect a large deviation of the tetrahedral environment of Fe nuclei from a spherical symmetry, which can be related to defect sites and/or very near the surface where the local symmetry is reduced. Higher values of σ -parameter also confirm this remark. More details on the relationship between QS and local symmetry in various iron-containing systems can be found elsewhere [29 – 31]. The third doublet with higher IS >0.5 mm/s is assigned to iron species in octahedral surroundings. Most likely, this component can be attributed to extra-framework ferrihydrite or ultra-dispersed hematite particles, for which room temperature Mossbauer spectra showed only a paramagnetic doublet [22,32].

**Table 5**
Hyperfine parameters obtained from the room-temperature $^{57}$Fe Mössbauer spectra for studied zeolites. Isomer shift (IS) is relative to α-Fe foil. <QS ≥ $e^2qQ/2$ and σ are the average quadrupole splitting and the Gaussian width of the QS distribution of the given spectral component, respectively.

| Sample | IS (mm/s) | <QS > (mm/s) | σ (μμ/σ) | Area (%) | Site |
|---|---|---|---|---|---|
| *$Fe_{2.5}Co_{2.5}$SiBEA* | 0.24 | 0.63 | 0.32 | 57 | $Fe^{3+}(T_d)_1$ |
| | 0.27 | 1.25 | 0.45 | 34 | $Fe^{3+}(T_d)_2$ |
| | 0.64 | 2.89 | 0.72 | 9 | $Fe^{3+}(O_h)_1$ |
| *$Fe_{5.0}Co_{5.0}$SiBEA* | 0.23 | 0.64 | 0.3 | 40 | $Fe^{3+}(T_d)_1$ |
| | 0.27 | 1.26 | 0.44 | 25 | $Fe^{3+}(T_d)_2$ |
| | 0.31 | 2.94 | 0.96 | 7 | $Fe^{3+}(O_h)_1$ |
| | | | | 28 | magnetic oxides |
| *$Fe_{10}Co_{10}$SiBEA* | 0.23 | 0.63 | 0.27 | 42 | $Fe^{3+}(T_d)_1$ |
| | 0.25 | 1.27 | 0.25 | 15 | $Fe^{3+}(T_d)_2$ |
| | 0.74 | 2.24 | 0.49 | 11 | $Fe^{3+}(O_h)_1$ |
| | | | | 32 | magnetic oxides |
| *$Fe_{2.5}Co_{2.5}$AlBEA* | 0.22 | 0.84 | 0.39 | 37 | $Fe^{3+}(T_d)_1$ |
| | 0.59 | 1.04 | 0.45 | 8 | $Fe^{3+}(O_h)_2$ |
| | 0.63 | 2.8 | 0.72 | 6 | $Fe^{3+}(O_h)_1$ |
| | | | | 49 | magnetic oxides |
| *$Fe_{5.0}Co_{5.0}$AlBEA* | 0.25 | 0.77 | 0.34 | 33 | $Fe^{3+}(T_d)_1$ |
| | 0.22 | 1.5 | 0.32 | 8 | $Fe^{3+}(T_d)_2$ |
| | 1.06 | 2.01 | 0.63 | 13 | $Fe^{2+}(O_h)_1$ |
| | | | | 46 | magnetic oxides |
| *$Fe_{10}Co_{10}$AlBEA* | 0.15 | 0.72 | 0.22 | 10 | $Fe^{3+}(T_d)_1$ |
| | 0.3 | 0.96 | 0.47 | 20 | $Fe^{3+}(T_d)_2$ |
| | 0.51 | 2.42 | 0.4 | 9 | $Fe^{3+}(O_h)_1$ |
| | | | | 61 | magnetic oxides |

As expected, the results show that the introduction of iron into the zeolite matrix is most effective for dealuminated BEA. >60% of the introduced Fe is located in intra-framework sites with tetrahedral symmetry, and in the case of $Fe_{2.5}Co_{2.5}$SiBEA it is as high as 91%. In the case of $Fe_xCo_y$AlBEA samples, only about 30–40% of the iron manages to incorporate into the zeolite framework. Remaining iron species are located in extra-framework positions mainly as $Fe_2O_3$ and $Fe_3O_4$ oxides.

The elemental composition of the surfaces of the studied samples was determined from their XPS survey spectra (Table S1, Supplementary Information). The absence of aluminum on the surface of dealuminated zeolites confirms the effectiveness of the method used. In the case of $Fe_{10}Co_{10}$SiBEA and $Fe_{5.0}Co_{5.0}$AlBEA samples, an enrichment of the surface in 3d metals (Fe and Co) compared to nominal values is observed.

High-resolution XPS spectra of Co 2p, Fe 2p and O 1 s lines (Fig. 5) were used to identify chemical bonds, and to determine the oxidation states of cobalt and iron, which made it possible to identify the chemical compounds present on the surface of the studied zeolites. Moreover, the spectra of the Si 2p lines (Fig. S4, Supplementary Information) provided information about the state of the zeolite matrix when 3d metals were introduced into it after dealumination or by wet impregnation. The appearance of the Si-O-Me bond indicates the incorporation of a certain amount of 3d metals into the zeolite framework. Carbon 1 s spectra (Fig. S5 and Table S2, Supplementary Information) showed atmospheric hydrocarbon and other contaminants present on the surfaces of samples exposed to the laboratory environment.

The comparison between the Fe 2p spectra acquired for $Fe_xCo_y$SiBEA and $Fe_xCo_y$AlBEA catalysts is shown in Fig. 5a. Complex spectral features of Fe 2p spectra can be found that are related to well-separated spin-orbit peaks with total momentum j = 3/2 and j = 1/2 overlapping by strong shake-up satellites in between. In addition, in the analysis of Fe 2p spectra, it is necessary to take into account the Auger line of Co LMM at BE close to 714 eV (Table 6). To describe the spectra correctly, two doublets and their accompanying four satellites must be used. Quite high Fe $2p_{3/2}$ binding energies (>710.5 eV) are characteristic for the ferric species and they are consistent with the values reported in the literature for Fe-BEA zeolites [33 – 37]. According to Yogo et al. [38], iron in the zeolite framework gives a higher BE peak than non-framework iron in the form of oxides like $Fe_3O_4$ or $Fe_2O_3$. It is related to the degree of dispersion of cations as well as to the interactions between them and the zeolite framework. One can conclude that high-BE component (~712 eV) can be assigned to ferric $Fe^{3+}$ ($T_d$) ions in the tetrahedral surroundings, thus embedded into the zeolite. The second component, with lower BE (~710.5 eV) most likely comes from non-framework iron oxides in the octahedral surroundings. The presence of strong satellites in measured spectra rather excludes a significant contribution of $Fe_3O_4$, since this oxide is characterized by almost complete satellite extinction [39]. In such a case, $Fe_2O_3$ is the most likely, which fully confirms Mössbauer results. Due to the fact, that BE has a little bit lower value than that reported for pure α-$Fe_2O_3$ to be around 711 eV [40], it cannot be excluded that some fraction of $Fe^{2+}$ species is also represented in this component. The spin–orbit splitting of Fe 2p lines for all samples is in the range of 12.9–13.5 eV and does not depend on how the samples are prepared. The quantitative share of framework and non-framework iron species is shown in the Table 6.

Co 2p XPS spectra (Fig. 5b) are composed of the two spin-orbit split peaks (charge transfer $2p^53d^8L^{-1}$ states) and their satellites (non-charge transfer $2p^53d^7$ states). Additional maxima, which overlap Co 2p lines, reflect Fe LMM Auger electron states (Table 6). The spin-orbit splitting of Co 2p doublets ~16 eV and the occurrence of strong shake up satellites are characteristic for high-spin $Co^{2+}$ ions. The satellites are shifted by 5–6 eV towards higher binding energies relative to the main

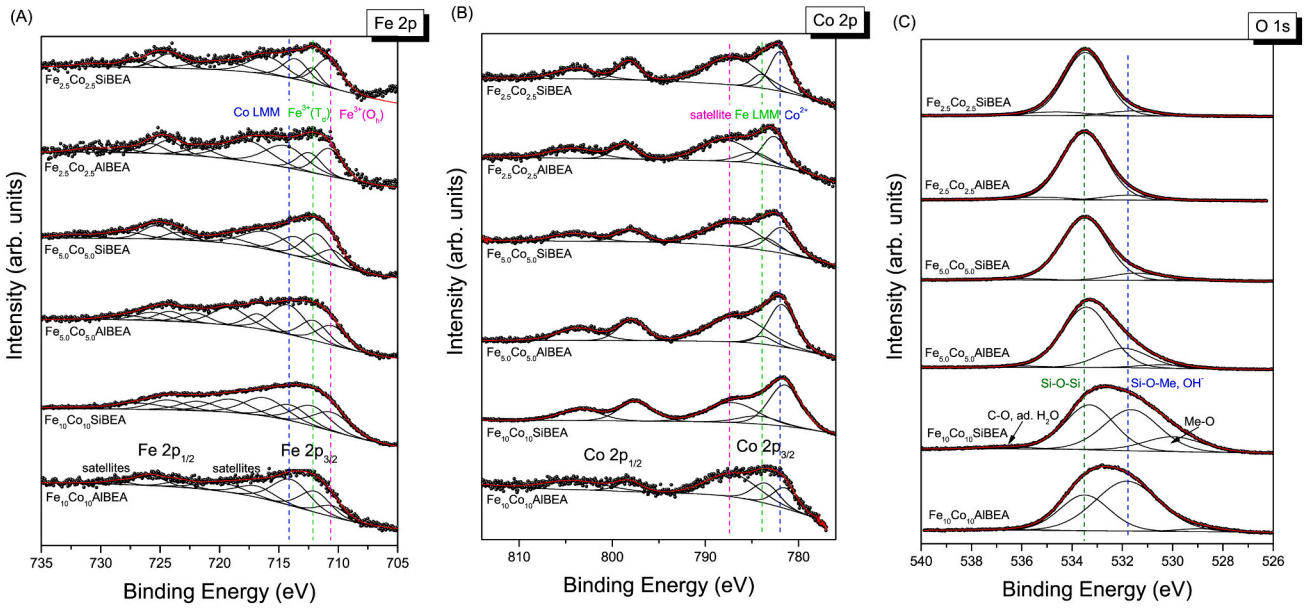


**Fig. 5.** XPS analysis of Fe 2p (A), Co 2p (B) and O 1 s (C) spectra for $Fe_xCo_ySiBEA$ and $Fe_xCo_yAlBEA$ zeolites. Dash lines are guides to the eye only.

**Table 6**
The BE values (eV) and relative areas of components (%) of Co $2p_{3/2}$, Fe LMM, Fe $2p_{3/2}$, Co LMM, O 1 s, Si $2p_{3/2}$ and Al $2p_{3/2}$ core excitations for studied zeolites.

| Core excitation | $Fe_{2.5}Co_{2.5}SiBEA$ | | $Fe_{5.0}Co_{5.0}SiBEA$ | | $Fe_{10}Co_{10}SiBEA$ | | $Fe_{2.5}Co_{2.5}AlBEA$ | | $Fe_{5.0}Co_{5.0}AlBEA$ | | $Fe_{10}Co_{10}AlBEA$ | |
|---|---|---|---|---|---|---|---|---|---|---|---|---|
| | BE (eV) | Area (%) | BE (eV) | Area (%) | BE (eV) | Area (%) | BE (eV) | Area (%) | BE (eV) | Area (%) | BE (eV) | Area (%) |
| Co $2p_{3/2}$ | 782.0 | 100 | 781.8 | 100 | 781.5 | 100 | 782.6 | 100 | 781.8 | 100 | 781.4 | 100 |
| Fe $2p_{3/2}$ | 710.8 | 75.7 | 710.5 | 32.4 | 710.5 | 49.1 | 710.8 | 59.8 | 710.5 | 51.2 | 710.5 | 32.4 |
| | 712.2 | 24.3 | 711.8 | 67.6 | 712.2 | 50.9 | 712.4 | 40.2 | 712.0 | 48.8 | 711.9 | 67.6 |
| Co LMM | 713.6 | | 713.6 | | 714.1 | | 714.5 | | 714.2 | | 714.0 | |
| Fe LMM | 784.0 | | 783.5 | | 784.3 | | 784.7 | | 783.9 | | 783.5 | |
| O 1 s | – | – | 529.5 | 1.4 | 530.0 | 15.7 | – | – | 530.4 | 11.4 | 528.9 | 2.5 |
| | 531.6 | 7.9 | 531.4 | 10.7 | 531.6 | 41.8 | 531.8 | 6.9 | 531.9 | 22.4 | 531.8 | 62.0 |
| | 533.5 | 84.6 | 533.5 | 85.9 | 533.3 | 40.5 | 533.5 | 88.8 | 533.4 | 64.7 | 533.5 | 34.4 |
| | 534.6 | 7.5 | 535.8 | 2.0 | 536.6 | 2.0 | 535.3 | 4.3 | 535.9 | 11.5 | 536.4 | 1.1 |
| Si $2p_{3/2}$ | 102.2 | 3.8 | 102.1 | 7.0 | 101.8 | 44.7 | 101.0 | 5.3 | 102.5 | 20.5 | 102.1 | 53.1 |
| | 104.0 | 96.2 | 103.9 | 93.0 | 103.8 | 55.3 | 103.7 | 94.7 | 103.9 | 79.5 | 103.8 | 46.9 |
| Al $2p_{3/2}$ | – | | – | | – | | 75.0 | 100.0 | 74.8 | 100 | 75.1 | 100.0 |

components. A single Co 2p doublet can indicate the presence of only one type of Co species on the surface of the catalysts tested. The BE values of Co $2p_{3/2}$ for bulk CoO and $Co_3O_4$ oxides, and for the hydroxide, $Co(OH)_2$, are respectively 780.1, 779.6 and 781.0 eV. In our samples, these energies are much higher and belong to the 781.4–782.6 eV range. In the case of $Co_3O_4$, which has a spinel structure and contains magnetic $Co^{2+}$ ions at tetrahedral sites and diamagnetic $Co^{3+}$ at octahedral sites, the two cobalt species are indistinguishable by XPS. However, it is well known that $Co_3O_4$ has weak satellites which occur about 7–9 eV higher from main peaks. Thus, both the positions of the main peaks and their satellites and the intensity of the satellites exclude the presence of simple oxides on the surface of zeolites. Most likely, cobalt is present as octahedral coordinated isolated divalent species in ion-exchanged positions. The Co $2p_{3/2}$ peaks with similar quite high BE values have also been assigned to bare $Co^{2+}$ ions at exchange positions in zeolites: CoBeta (782.5 eV) [41], CoFER (782.7 eV) [42], $Co^{2+}$-exchanged NaY (782.3 eV) [43], and Co-ZSM-5 (782.4 eV) [44]. In the case of this latter zeolite, a mechanism for the formation of octahedrally coordinated $Co^{2+}$ species in amorphous micro-aggregates of the hydrated form $[Co(H_2O)_6]^{2+}$ was proposed by Chupin et al. [45].

It is worth mentioning that with increasing cobalt content in the samples, binding energies of Co $2p_{3/2}$ peak move towards lower values. It means, that with an increase in the amount of cobalt in the samples, a more amount of oxide, presumably $Co_3O_4$, is formed. This result confirms the observations made by XRD. Moreover, the speciation of cobalt on the surface of BEA zeolite is independent of preparation method.

XPS O 1 s spectra of zeolites with the least amount of introduced 3d metals can be fitted by three components (Fig. 5c). The most intense component with a binding energy of ~533.5 eV can be attributed to oxygen in the zeolite framework [46 – 50]. Si-O-Me bonds as well as some hydroxyls on the zeolite surface are visible in the spectra as a signal located at BE of ~531.6 eV. This component increases significantly with an increase in the amount of 3d metal introduced into the zeolite matrix. Small contribution at high BE (>534.6 eV) is related to adsorbed water and/or oxygen of organic contaminants. Samples containing higher amounts of Co and Fe, in addition to the components listed above, have an additional low-BE component derived from Me-O bonds. The BE positions of the lattice oxygen in cobalt oxides CoO, $Co_3O_4$, and $Co(OH)_2$ are located at 529.2, 529.6, and 530.1 eV, respectively [51]. Also in this range one can find lattice oxygen derived from iron oxides $Fe_2O_3$ (530.1 eV) and γ-FeOOH (529.8 eV) [52] or Fe3O4 (530.0 eV) [53]. Thus, Me-O bonds with binding energies in the 528.9–530.4 eV range can be assumed to originate from extra-framework cobalt and iron oxides. The proportion of the Me-O bond is highest for $Fe_{5.0}Co_{5.0}AlBEA$ and $Fe_{10}Co_{10}SiBEA$, which is consistent with the enrichment in 3d metals on the zeolite surface observed in their XPS survey spectra. The quantitative contribution of each bond to the

total spectral area can be found in Table 6.

### 3.4. Catalytic activity

The catalytic activity of bimetallic iron-cobalt BEA zeolite catalysts was studied at 300 °C (this temperature was chosen after optimizing the process on Red-C-$Fe_{10}Co_{10}$AlBEA catalysts at 260, 300 and 340 °C, and based on the catalytic performance on Red-C-CoSiBEA and Red-C-FeSiBEA monometallic catalysts described in our previous work [9,10]) under an elevated pressure of 30 atm and an $H_2$ to CO ratio of 2. Before testing the catalytic performance, all catalysts were subjected to *in situ* reduction in hydrogen flow for 1 h at 400 °C selected on the basis of TPR and XRD measurements, which showed that reduction at this temperature leads to a mainly metallic iron phase. At this temperature, iron oxides and partially also cobalt oxides, which are located in the extra-framework positions, are reduced.

Figs. 6–10 show the results of catalytic performance. The results of the catalytic activity are also summarized in Table 7. Fig. 6 presents the results after 20 h of reaction for all the FeCoBEA bimetallic zeolite catalysts studied and showed the difference between the samples obtained by various preparation methods. These results indicate that carbon monoxide conversion and selectivity to liquid products increase with increasing metal loading in the samples (Fig. 6).

The water is one of the main product of FTS process and it should be mentioned that in both cases of cobalt and iron catalysts the presence of water can have positive and negative influence. It is known that in the case of monometallic supported cobalt catalysts could have positive effect on CO conversion, olefins and $C_{5+}$ selectivities [55]. In the case of monometallic iron catalysts the water effect is better known and understood as reoxidises iron during FTS and decrease the syngas consumption rate [56]. In our studies using the bimetallic iron-cobalt catalysts in FTS is is likely the overlap of these two effects so from the one side the high CO conversion led to higher level of water and the same higher partial pressure of water what can improve the selectivities to $C_{5+}$ hydrocarbons and the improvement of propagation of chain growth could be partially assigned to influence of water presence. However, it was also observed the slightly decrease of CO conversion in compare to monometallic cobalt catalysts what suggests that the presence of water can affect to reoxidise of iron localized in extra-framework position of BEA zeolite. The role of water in activity of bimetallic FeCoBEA zeolite catalysts is still not well understood and demand to carry out more detailing studies.

The most active catalyst with the highest CO conversion (close to 81%) and the highest selectivity to liquid products (close to 77%) was Red-C-$Fe_{10}Co_{10}$SiBEA. It should be mentioned that the selectivity to liquid hydrocarbons is about 6% higher for dealuminated catalysts compared to non-dealuminated samples. Similarly, selectivity to gaseous hydrocarbons $C_1$-$C_4$, an undesired products, is lowest for the most active catalyst, Red-C-$Fe_{10}Co_{10}$SiBEA. It seems that the

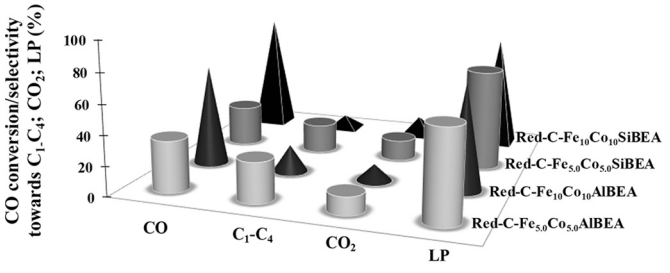


**Fig. 6.** Conversion of carbon monoxide and selectivity towards methane, carbon dioxide and liquid products during FTS process carried out at 300 °C under pressure of 30 atm and 20 h using bimetallic Red-C-FeCoAlBEA and Red-C-FeCoSiBEA zeolite catalysts. (For interpretation of the references to colour in this figure legend, the reader is referred to the web version of this article.)

dealumination process in the first stage of the preparation of these catalysts may affect the decrease in selectivity to these hydrocarbons. It should be highlighted that the value of selectivity to $C_1$-$C_4$ found for bimetallic samples is lower than that recorded for monometallic cobalt BEA zeolite catalysts and at the same level as that noted for monometallic FeSiBEA catalysts. The selectivity towards $CO_2$ recorded for the dealuminated Red-C-$Fe_xCo_y$SiBEA catalysts was about 14%, and for the non-dealuminated Red-C-$Fe_xCo_y$AlBEA series was about 11–12%, these values are slightly higher than those determined for the monometallic cobalt BEA zeolites (10%), but also slightly lower than those for monometallic iron SiBEA zeolites catalysts (16–18%) [9,10]. This can suggest that the preparation of bimetallic FeCoBEA zeolite catalysts can lead to combining the advantages of monometallic iron and cobalt catalysts and minimizing their disadvantages. Moreover, all tested catalysts were very stable and did not show any changes in their activity and selectivity throughout the reaction (Fig. 7).

The fraction of liquid products was analyzed by GC – MS. The results are presented in the Figs. 8 and 9, while the quantitative analysis is shown in Table 7. In the FT reaction carried out on Red-C-$Fe_xCo_y$SiBEA catalysts, the main liquid products are isoalkanes and saturated hydrocarbons ($C_{10}$ – $C_{20}$ for samples with 2.5 wt% of Co and Fe (Fig. 9) and 5 wt% of Co and Fe (Fig. 8a) and $C_{10}$ – $C_{24}$ for the sample with the highest metal loading – Fig. 8b). The ratio of isoalkanes to n-alkanes is the highest at 2.96 for Red-C-$Fe_{10}Co_{10}$SiBEA (Fig. 8b and Table 7), 2.27 for Red-C-$Fe_{2.5}Co_{2.5}$SiBEA (Fig. 9) and 1.57 for Red-C-$Fe_{5.0}Co_{5.0}$SiBEA (Fig. 8a and Table 7). It should be mentioned that levels of CO conversion and liquid product selectivity for Red-C-$Fe_{2.5}Co_{2.5}$SiBEA were very low and unsatisfactory, not higher than 5%, so this sample could not be considered a good catalyst for Fischer-Tropsch synthesis despite the good composition of liquid hydrocarbons and their percentages [12]. In the case of the FT reaction performed on non-dealuminated bimetallic iron–cobalt BEA zeolite catalysts, isoalkanes and n-alkanes were also identified. However, for the catalyst with the highest metal loading, more diverse products were observed. For the Red-C-$Fe_{10}Co_{10}$AlBEA sample, the ratio of isoalkanes to n-alkanes is 2.52 (Fig. 8d), but other products such as aromatic hydrocarbons (ratio to n-alkanes is 1.5), cycloalkanes (ratio to n-alkanes is 0.5), n-alkenes – olefins (ratio to n-alkanes is 0.4) and oxidized products (ratio to n-alkanes is 0.73) were also observed. The number of carbons in these identified products is $C_9$ – $C_{18}$. This is likely due to the large amount of iron ions present in the extra-framework positions and channels of the AlBEA zeolite, since iron catalysts in FTS are usually responsible for the formation of oxidized liquid products. In the Red-C-$Fe_{5.0}Co_{5.0}$AlBEA sample, where the ratio of surface $Fe^+$ to $Co^+$ ions is lower than that identified for the sample with higher metal loading, only alkanes and isoalkanes with $C_9$ – $C_{23}$ in the chains were observed, and the ratio of isoalkanes to n-alkanes is 0.79 [Fig. 8c and Tabel 7). Similarly, for the Red-C-$Fe_xCo_y$SiBEA series of catalysts, the ratio of surface $Fe^+/Co^+$ calculated from ToF-SIMS data was lower, and the identified liquid products were also mainly alkanes and isoalkanes, more characteristic for monometallic cobalt catalysts. However, it seems that such a high ratio of isoalkanes to n-alkanes for all Red-C-$Fe_xCo_y$SiBEA bimetallic catalysts (higher than for monometallic catalysts described in our earlier work) may be related to the presence of different cobalt species and its localization in the pseudo-tetrahedral positions and its replacement by aluminum oxide, which caused the formation of new acidic sites and gave new catalytic properties to the BEA zeolite, and in these new active sites the isomerization process could take place. It is known that the presence of Brønsted acidic sites promotes aromatization reactions, while the reduction in the number of these acidic centers and the formation of more Lewis acidic sites favour the formation of isoalkanes and alkanes [54].

An important problem in Fischer–Tropsch synthesis is carbon deposition, which blocks the active sites of the reaction. We investigated the type and amount of carbon deposition by TG – DTA – MS technique. The results are presented in Fig. 10 and Table 7. Temperature-programmed oxidation was performed to determine the type of coke

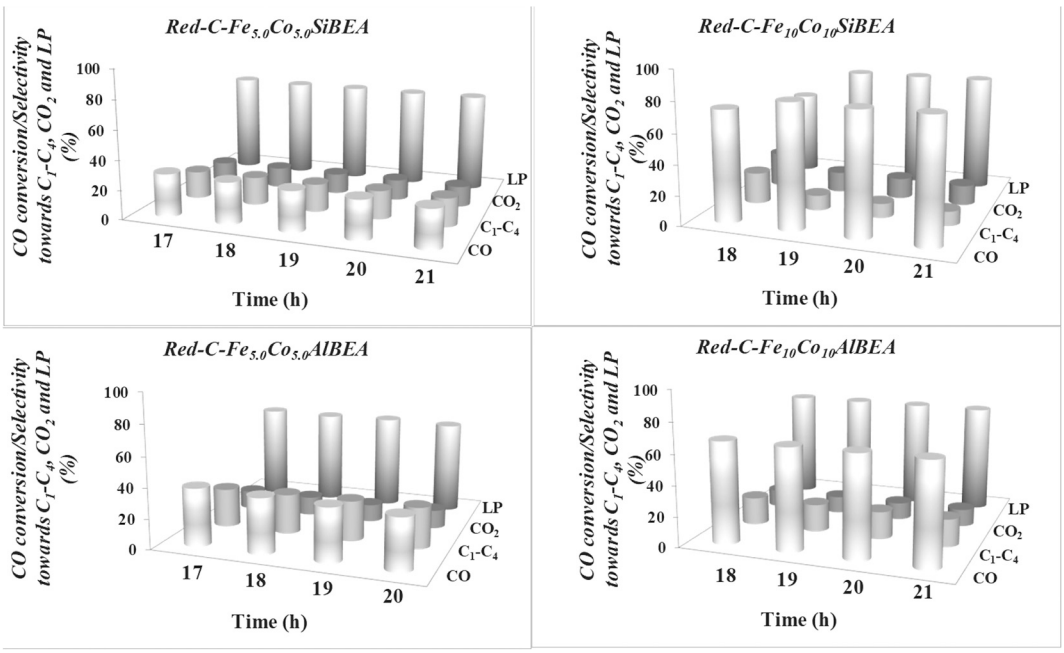


**Fig. 7.** Catalytic activity, selectivity and stability of bimetallic Red-C-FeCoSiBEA and Red-C-FeCoAlBEA zeolite catalysts in FTS process. (For interpretation of the references to colour in this figure legend, the reader is referred to the web version of this article.)

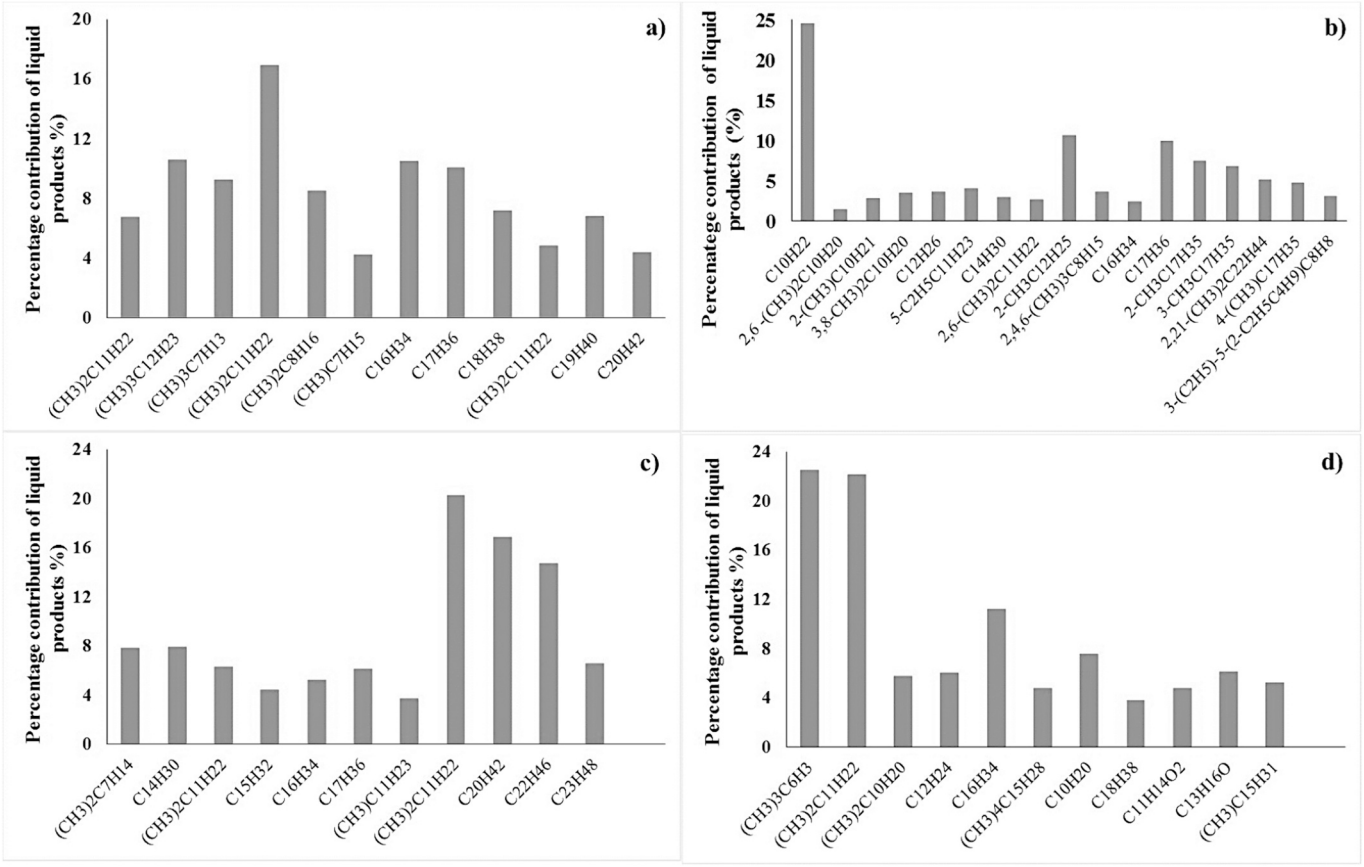


**Fig. 8.** GC–MS analysis of liquid products obtained in FTS process at 300 °C for 20 h on a) Red-C-$Fe_{5.0}Co_{5.0}$SiBEA; b) Red-C-$Fe_{10}Co_{10}$SiBEA; c) Red-C-$Fe_{5.0}Co_{5.0}$AlBEA and d) Red-C-$Fe_{10}Co_{10}$AlBEA catalysts calcined at 500 °C for 3 h and reduced in 400 °C for 1 h. (For interpretation of the references to colour in this figure legend, the reader is referred to the web version of this article.)

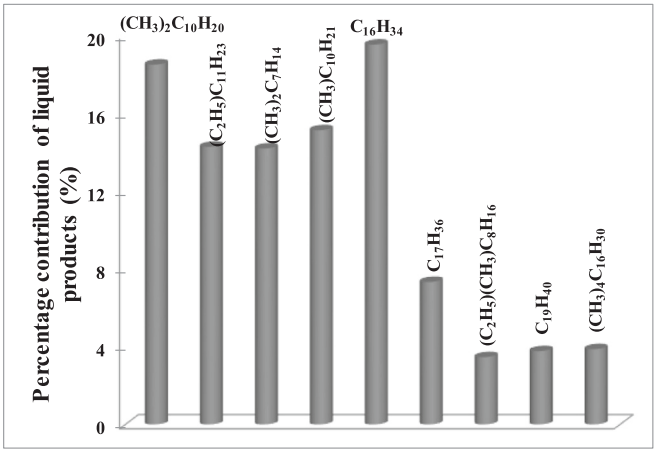


**Fig. 9.** GC – MS analysis of liquid products obtained in FTS process at 300 °C for 20 h on Red-C-$Fe_{2.5}Co_{2.5}$SiBEA catalyst calcined at 500 °C for 3 h and reduced in 400 °C for 1 h. (For interpretation of the references to colour in this figure legend, the reader is referred to the web version of this article.)

deposition.

Carbon oxidation occurs in the temperature range 200–600 °C for a series of dealuminated catalysts and is shifted to slightly higher temperatures for non-dealuminated samples, suggesting the presence of different kinds of carbon species that are relatively easy to oxidize. The broad peak is probably related to the removal of various carbides or waxes and polymeric carbon that may be present on the surface of the support. It is noteworthy that the amount of carbon deposition decreases for dealuminated Red-C-$Fe_xCo_y$SiBEA catalysts by almost 2 times in contrast to non-dealuminated Red-C-$Fe_xCo_y$AlBEA samples, indicating that the dealumination process improves carbon deposition resistance. In addition, the amount of carbon deposition noted for dealuminated bimetallic Red-$Fe_xCo_y$SiBEA catalysts is also 2 times lower than the amount of carbon deposition described in our previous work for monometallic FeSiBEA catalysts and only a few percent higher than that observed for monometallic CoSiBEA catalysts. This confirms that the combination of iron and cobalt in a single catalytic system can be a good solution for reducing the cost of synthesis and improving the process parameters, since the combination of iron and cobalt allows for a lower loading of cobalt, which is more expensive than iron, but at the same time the presence of cobalt leads to less carbon deposition, as well as the use of lower reaction temperature, resulting in a more economical process. In addition, the preparation of bimetallic cobalt-iron catalysts supported on BEA zeolite provides lower selectivity towards undesired products, such as $CO_2$ (selectivity was lower than for monometallic iron catalysts) and $C_1$-$C_4$ hydrocarbons (selectivity was slightly lower than for monometallic cobalt catalysts) and higher CO conversion compared to monometallic iron catalysts, as well as lower carbon deposition than reported for monometallic iron catalysts.

## 4. Conclusions

Two types of bimetallic iron-cobalt Beta zeolite catalysts obtained by two different methods – the classical wet sequential impregnation ($Fe_xCo_y$AlBEA) and the two-step post-synthesis method ($Fe_xCo_y$SiBEA) - have been investigated for their potential application in Fischer-Tropsch synthesis, and the conclusions are as follows:

- The volume of micropores for all C-$Fe_xCo_y$AlBEA catalysts was similar, and the average pore radius decreased slightly, which can suggest that some metallic species or ions are localized inside the pores of the AlBEA zeolite;
- The shape of the pore distribution curves indicates that the surface area of C-FeCoSiBEA decreases with increasing metal loading, and suggests that metal particles agglomerate on the external support surface in C-FeCoSiBEA samples;
- XRD results indicate a slight shrinkage of the matrix under HAlBEA dealumination and expansion after metal ion incorporation into the SiBEA structure, and prove that the BEA zeolite structure is preserved after dealumination and metal incorporation processes;
- The small percentage of the $Co_3O_4$ phase in the case of C-$Fe_xCo_y$SiBEA samples suggests that cobalt ions react with the silanol groups of

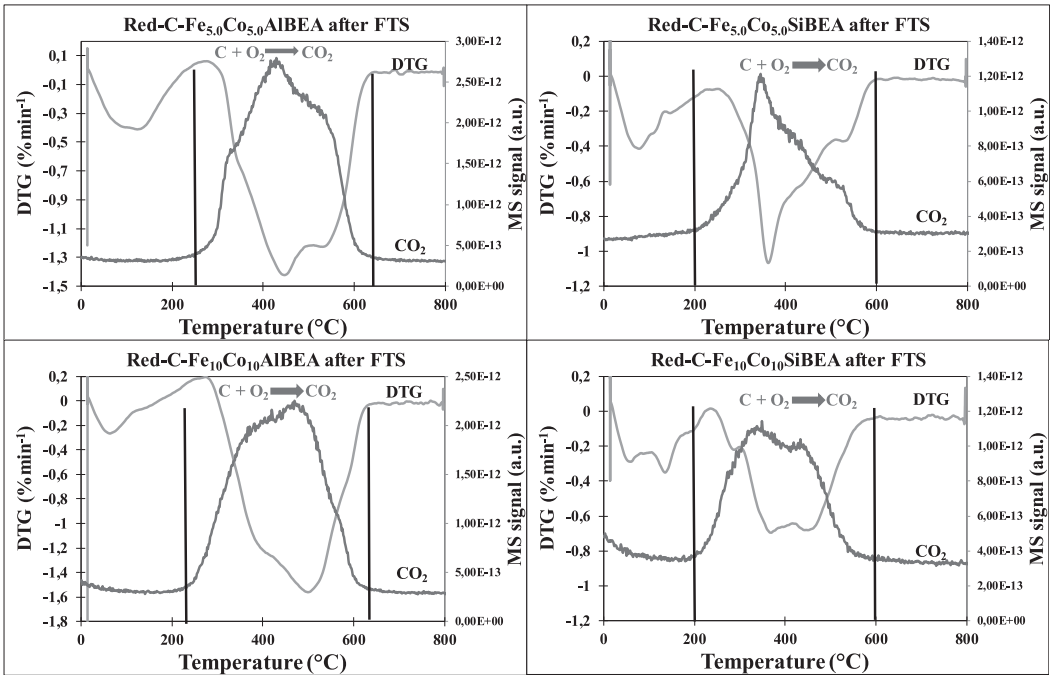


**Fig. 10.** The TG-DTA-MS profiles for Red-C-$Fe_{5.0}Co_{5.0}$AlBEA; Red-C-$Fe_{10}Co_{10}$AlBEA; Red-C-$Fe_{5.0}Co_{5.0}$SiBEA and Red-C-$Fe_{10}Co_{10}$SiBEA samples after FTS process. (For interpretation of the references to colour in this figure legend, the reader is referred to the web version of this article.)

**Table 7**
The catalytic activity and selectivity of bimetallic iron-cobalt BEA zeolite catalysts in Fischer-Tropsch synthesis (T = 300 °C, p = 30 atm, t = 20 h).

| Samples | Red-C-$Fe_{5.0}Co_{5.0}$SiBEA | Red-C-$Fe_{5.0}Co_{5.0}$AlBEA | Red-C-$Fe_{10}Co_{10}$SiBEA | Red-C-$Fe_{10}Co_{10}$AlBEA | Monometallic Red-C-$Co_{20}$SiBEA*/ Red-C-$Fe_{20}$SiBEA** |
|---|---|---|---|---|---|
| CO conversion (%) | 27.1 | 34.4 | 81.0 | 67.2 | 97/62 |
| Selectivity towards liquid products – $C_{5+}$ (%) | 66.7 | 60.7 | 76.8 | 70.7 | 84/70 |
| Selectivity towards $C_1$ – $C_4$ (%) | 19.4 | 27.2 | 9.6 | 18.1 | 11/15 |
| Selectivity towards $CO_2$ (%) | 13.9 | 12.2 | 13.6 | 11.2 | 5/16 |
| Yield of reaction (to liquid hydrocarbons) $C_{5+}$ (%) | 18.1 | 20.9 | 62.2 | 47.5 | – |
| $\alpha_{C5+}$ | 0.89 | 0.97 | 0.89 | 0.85 | – |
| Carbon deposition | 12.8 | 29.9 | 18.1 | 31.7 | 12.4/35.4 |
| Iso−/n-alkanes ratio | 1.57 | 0.79 | 2.96 | 2.52 | 0.28/0.87 |
| Other products to n-alkanes ratio | – | – | – | Aromatic/n-alkanes: 1.50<br>Cycloalkanes/n-alkanes: 0.5<br>n-alkene/n-alkanes: 0.40<br>oxidative products/n-alkanes: 0.73 | |
| Co nanoparticles size after FTS (nm)*** | 14 | 16 | 17 | 5 | |
| Fe nanoparticles size after FTS (nm)*** | 21 | 8 | 17 | 20 | |

* Data from Ref. [9].
** Data from Ref. [10].
*** Average crystallite size was calculated from XRD peak broadening using the Scherrer equation (XRD measurement for used samples (after FTS)).

vacant T-atom sites and are incorporated into the framework of the zeolite structure, thus creating new catalytic properties;
- The ToF-SIMS results proved that the dealumination process was successful and confirmed that Co in the C-$Fe_xCo_y$SiBEA samples is mainly present in the framework positions of the BEA zeolite and only excess of cobalt is present in the extra-framework positions;
- For both series of catalysts, the main liquid products are isoalkanes and n-alkanes, but a number of oxidized products, aromatic hydrocarbons, olefins and cycloalkanes were also identified for the non-dealuminated catalyst with the highest metal loading (Red-C-$Fe_{10}Co_{10}$SiBEA), suggesting that the type and amount of liquid products are related to the presence of different types of acidic sites in the dealuminated and non-dealuminated catalysts;
- The iso−/n-alkanes ratio for bimetallic catalysts with dealuminated zeolites is twice as high as for the described monometallic CoSiBEA,
- Selectivity towards $C_1$–$C_4$ and towards $CO_2$ observed for bimetallic Red-C-FeCoSiBEA catalysts is lower than for monometallic zeolite BEA catalysts with cobalt and iron, which can suggest that bimetallic iron-cobalt BEA zeolite catalytic systems combine the advantages of monometallic catalysts, such as lower selectivity towards undesired gaseous products, while minimizing their disadvantages, such as high carbon deposition.

## CRediT authorship contribution statement

**Karolina A. Chałupka-Śpiewak:** Conceptualization, Data curation, Investigation, Methodology, Project administration, Writing – original draft, Writing – review & editing. **Jacek Gurgul:** Investigation, Methodology, Writing – review & editing. **Jacek Grams:** Data curation, Investigation. **Paweł Mierczyński:** Investigation. **Waldemar Maniukiewicz:** Investigation. **Małgorzata I. Szynkowska-Jóźwik:** Formal analysis, Resources. **Kazimierz Łątka:** Investigation, Methodology, Writing – review & editing. **Jacek Rynkowski:** Formal analysis, Supervision. **Stanisław Dźwigaj:** Methodology, Supervision, Writing – review & editing.

## Declaration of competing interest

The authors declare that they have no known competing financial interests or personal relationships that could have appeared to influence the work reported in this paper.

## Data availability

Data will be made available on request.

## Acknowledgments

Karolina Chałupka-Śpiewak acknowledges for the financial support in 2014, 2015 and 2017 from Fund of Young Scientists of Faculty of Chemistry in Lodz University of Technology (grant of Dean of Faculty of Chemistry for Young Researchers).

## Appendix A. Supplementary data

Supplementary data to this article can be found online at https://doi.org/10.1016/j.apcato.2024.206935.

## References

[1] R.Y. Abrokwah, M.M. Rahman, V.G. Deshmane, D. Kuila, Mol. Catal. 478 (2019) 110566.
[2] L.F.F.P.G. Bragança, M. Ojeda, J.L.G. Fierro, M.I. Pais da Silva, Appl. Catal. A: General 423–424 (2012) 146.
[3] S. Logdberg, Appl. Catal. B Environ. 89 (2009) 167.
[4] E. van Steen, M. Claeys, Chem. Eng. Technol. 31 (2008) 655.
[5] W. D. Shafer, M. K, Gnanamani, U. M. Graham, J. Yang, C. M. Masuku, G. Jacobs, B. H. Davis, Catalysts 9 (2019) 259.
[6] P. K. Gupta S. Mandal, A. Mahato, S. Maity, Indian J. Chem. Technol. 26 (2019) 337.
[7] A.A. Khassin, I. Pechenyuk, D.P. Domonov, T.P. Minyukova, G. K. Chermashentseva, G.N. Kustova, L.M. Plyasova, Chem. Sustain. Dev. 15 (2007) 673.
[8] A.M. Saib, D.J. Moodley, I.M. Ciobica, M.M. Hauman, B.H. Sigwebela, C. J. Weststrate, J.W. Niemantsverdriet, J. van der Loosdrecht, Catal. Today 154 (2010) 271.
[9] K.A. Chalupka, S. Casale, E. Zurawicz, J. Rynkowski, S. Dzwigaj, Microporous Mesoporous Mater. 211 (2015) 9.
[10] K.A. Chalupka, W. Maniukiewicz, P. Mierczyński, T. Maniecki, J. Rynkowski, S. Dzwigaj, Catal. Today 257 (2015) 117.
[11] R. Sadek, K.A. Chalupka, P. Mierczynski, J. Rynkowski, Y. Millot, L. Valentin, S. Casale, S. Dzwigaj, Catal. Today 354 (2020) 109.
[12] S. Dzwigaj, M.J. Peltre, P. Massiani, A. Davidson, M. Che, S. Dzwigaj, P. Massiani, T. Sen, S. Sivasanker, Chem. Commun. (1998) 87.
[13] G.J. Long, T.E. Cranshaw, G. Longworth, Mössbauer Effect Reference and Data Journal 6 (1983) 42–49.
[14] D.G. Rancourt, J.Y. Ping, Nucl. Inst. Methods Phys. Res. B 58 (1991) 85–97.
[15] M. Thommes, Chem. Ing. Tech. 82 (2010) 1059.
[16] K.A. Chalupka, J. Grams, P. Mierczynski, M.I. Szynkowska, J. Rynkowski, T. Onfroy, S. Casale, S. Dzwigaj, Catalysts 10 (2020) 553.

[17] R. Sadek, K.A. Chalupka, P. Mierczynski, J. Rynkowski, J. Gurgul, S. Dzwigaj, Catalysts 9 (2019) 497.
[18] S. Dzwigaj, M. Che, J. Phys. Chem. B 110 (2006) 12490.
[19] O.J. Wimmers, P. Arnoldy, J.A. Moulijn, J. Phys. Chem. 90 (1986) 1331.
[20] J. Zieliński, I. Zglinicka, L. Znak, Z. Kaszkur, Appl. Catal. A 381 (2010) 191.
[21] C.–I. Ahn, H. Mo Koo, K.-S. Ha, J. Jeon, J. Min Cho, Y.-B. Kim, G. Young Han, J. Lee, C.-H. Shin, J. Wook Bae, ChemCatChem 12 (2020) 2304.
[22] J. Fock, M.F. Hansen, C. Frandsen, S. Mørup, J. Magn. Magn. Mater. 445 (2018) 11.
[23] W. Kundig, H. Bommel, G. Constabaris, R.H. Lindquist, Phys. Rev. 142 (1966) 327–333.
[24] R.G. Burns, Hyperfine Interact. 91 (1994) 739.
[25] M. Zimowska, J. Gurgul, H. Palkova, Z. Olejniczak, K. Łątka, L. Lityńska-Dobrzyńska, L. Matachowski, Microporous Mesoporous Mater. 231 (2016) 66.
[26] P. Fejes, J.B. Nagy, K. Lázár, J. Halász, Appl. Catal. A 190 (2000) 117.
[27] A.M. van der Kraan, Phys. Status Solidi (a) 18 (1973) 215.
[28] R.M. Mihalyi, K. Lazar, M. Kollar, F. Lonyi, G. Pal-Borbely, A. Szegedi, Microporous Mesoporous Mater. 110 (2008) 51.
[29] J. Gurgul, E. Młyńczak, N. Spiridis, J. Korecki, Surf. Sci. 606 (2012) 711.
[30] M. Zimowska, K. Łątka, D. Mucha, J. Gurgul, L. Matachowski, J. Mol. Catal. A 423 (2016) 92.
[31] M.G. Shelyapina, J. Gurgul, K. Łątka, P. Sanchez-Lopez, D. Bogdanov, Y. Kotolevich, V. Petranovskii, S. Fuentes, Microporous Mesoporous Mater. 299 (2020) 109841.
[32] L. Machala, R. Zboril, A. Gedanken, J. Phys. Chem. B 111 (2007) 4003–4018.
[33] J. Janas, J. Gurgul, R.P. Socha, T. Shishido, M. Che, S. Dźwigaj, Appl Catal B 91 (2009) 113.
[34] J. Gurgul, K. Łątka, I. Hnat, J. Rynkowski, S. Dźwigaj, Microporous Mesoporous Mater. 168 (2013) 1.
[35] P. Boroń, L. Chmielarz, J. Gurgul, K. Łątka, T. Shishido, J.-M. Krafft, S. Dzwigaj, Appl Catal B 138–139 (2013) 434.
[36] P. Boroń, L. Chmielarz, J. Gurgul, K. Łątka, B. Gil, J.-M. Krafft, S. Dźwigaj, Catal. Today 235 (2014) 210.
[37] P. Boroń, L. Chmielarz, J. Gurgul, K. Łątka, B. Gil, B. Marszałek, S. Dzwigaj, Microporous Mesoporous Mater. 203 (2015) 73.
[38] K. Yogo, S. Tanaka, T. Ono, T. Mikami, E. Kikuchi, Microporous Mesoporous Mater. 3 (1994) 39.
[39] M. Descostes, F. Mercier, N. Thromat, C. Beaucaire, M. Gautier-Soyer, Appl. Surf. Sci. 165 (2000) 288.
[40] T. Fujii, F.M.F. de Groot, G.A. Sawatzky, F.C. Voogt, T. Hibma, K. Okada, Phys. Rev. B 59 (1999) 3195.
[41] H.-H. Chen, S.-C. Shen, X. Chen, S. Kawi, Appl Catal B 50 (2004) 37.
[42] A.V. Boix, J.M. Zamaro, E.A. Lombardo, E.E. Miro, Appl Catal B 46 (2003) 121.
[43] Z. Zsoldos, G. Vass, G. Lu, L. Guczi, Appl. Surf. Sci. 78 (1994) 467.
[44] R.S. Da Cruz, A.J.S. Mascarenhas, H.M.C. Andrade, Appl Catal B 18 (1998) 223.
[45] C. Chupin, A.C. Van Veen, M. Konduru, J. Despres, C. Mirodatos, J. Catal. 241 (2006) 103.
[46] I. Kocemba, J. Rynkowski, J. Gurgul, R.P. Socha, K. Łątka, J.-M. Krafft, S. Dzwigaj, Appl. Catal. A 519 (2016) 16.
[47] N.O. Popovych, P.I. Kyriienko, Y. Millot, L. Valentin, J. Gurgul, R.P. Socha, J. Żukrowski, S.O. Soloviev, S. Dzwigaj, Microporous Mesoporous Mater. 268 (2018) 178.
[48] E.R. Bandala, R. Sadek, J. Gurgul, K. Łątka, M. Zimowska, L. Valentin, O. M. Rodriguez-Narvaez, S. Dzwigaj, Chem. Eng. J. 409 (2021) 127379.
[49] K. Pamin, J. Gurgul, G. Mordarski, Y. Millot, J.-P. Nogier, L. Valentin, S. Dzwigaj, Microporous Mesoporous Mater. 322 (2021) 111159.
[50] S. Orlyk, P.I. Kyriienko, A. Kapran, V. Chedryk, D. Balakin, J. Gurgul, Y. Millot, M. Zimowska, S. Dzwigaj, Catalysts 13 (2023) 681.
[51] M. Martinez-Gil, D. Cabrera-German, M.I. Pintor-Monroy, J.A. Garcia-Velenzuela, M. Cota-Leal, W. De la Cruz, M.A. Quevedo-Lopez, R. Perez-Salas, M. Sotelo-Lerma, Mater. Sci. Semicond. Process. 107 (2020) 104825.
[52] H. Abdel-Samad, P.R. Watson, Appl. Surf. Sci. 108 (1997) 371.
[53] L. Martinez, D. Leinen, F. Martín, M. Gabas, J.R. Ramos-Barrado, E. Quagliata, E. A. Dalchiele, J. Electrochem. Soc. 154 (2007) D126.
[54] A. Martinez, C. Lopez, Appl. Catal. A 294 (2005) 251.
[55] A.K. Dalai, B.H. Davis, Appl. Catal. A 348 (2008) 1.
[56] D.B. Bukur, B. Todic, N. Elbashir, Catal. Today 275 (2016) 66.